CHALMERS
UNIVERSITY OF TECHNOLOGY

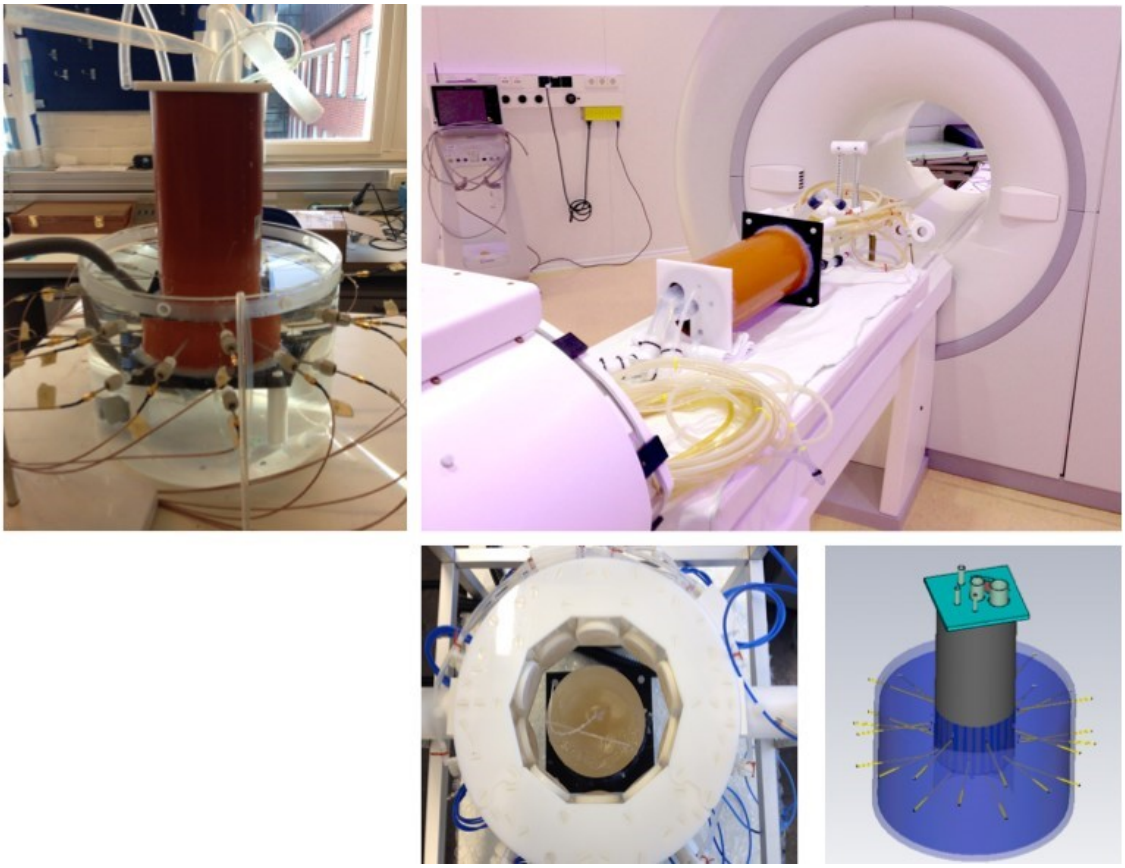

Non-Invasive Thermometry for Microwave Hyperthermia: Evaluation of MW-Thermometry

Master's thesis in Biomedical Engineering

Masoud Shafiemehr

Department of Signals and Systems
CHALMERS UNIVERSITY OF TECHNOLOGY
Gothenburg, Sweden 2015

Master's thesis 2015:NN

Non-Invasive Thermometry for Microwave Hyperthermia:

Evaluation of MW-Thermometry

Masoud Shafiemehr

CHALMERS
UNIVERSITY OF TECHNOLOGY

Department of Signals and Systems
Biomedical Electromagnetics Group Chalmers
Chalmers University of Technology
Gothenburg, Sweden 2015

Non-Invasive Thermometry for Microwave Hyperthermia:
Evaluation of MW-Thermometry
Masoud Shafiemehr

Supervisor: Hana Dobsicek Trefna, Department of Signals and Systems
Examiner: Andreas Fhager, Department of Signals and Systems

Master's Thesis 2015:NN
Department of Signals and Systems
Biomedical Electromagnetics Group Chalmers
Chalmers University of Technology
SE-412 96 Gothenburg
Telephone +46 31 772 1000

Cover: The MR-thermometry experimental setup (top right), the MW-thermometry experimental setup (top left), the experimental HT applicator (bottom left) and the simulated MW-thermometry system in CST-STUDIO (bottom right).

Typeset in LaTeX
Gothenburg, Sweden 2015

Non-Invasive Thermometry for Microwave Hyperthermia:
Evaluation of MW-Thermometry
Masoud Shafiemehr
Department of Signals and Systems
Chalmers University of Technology

Abstract

The importance of non-invasive temperature monitoring during microwave hyperthermia treatment has motivated the development of non-invasive thermometry (NIT) methods. Currently, the clinically established method for NIT is magnetic resonance thermometry (MRT). This method has however some limitations such as high costs, high sensitivity to patient motion and the requirement of a large installation space.
Microwave tomography became of interest for thermal monitoring during hyperthermia treatment recently. The work in this thesis is aimed at investigating microwave tomography for 3D thermal mapping with the same antenna array used for heating. MRT was used as a reference method to evaluate the accuracy of microwave thermometry (MWT).
This study uses two antenna arrays developed at Chalmers University of Technology with the aim of investigating the feasibility of MWT. Both simulations and experiments with two antenna systems were performed on a phantom specifically developed for this study to gain a better understanding of how these two systems affect the results. In addition, the metric Good Data Ratio (GDR) was evaluated and applied to the obtained data in the MWT method. Finally, experimental measurements with MRT were performed to evaluate the temperature resolution and accuracy in comparison with MWT.

Keywords: magnetic resonance thermometry (MRT), microwave thermometry (MWT), fast 3D image reconstruction, good data ratio (GDR), PRFS α-parameter calibration.

Acknowledgements

Many people gave me support and assistance for my thesis work. I would like to express my deep appreciation to them.

My biggest gratitude goes to my supervisor Hana Dobsicek Trefna for her great support and friendly guidance. She provided me with the freedom to test and realize my ideas, and gave me encouragement and valuable guidance when I faced troubles. I would also like to thank my examiner Andreas Fhager for the useful comments, remarks and engagement through the learning process of microwave tomography.

A huge thanks to Pegah for helping me during this thesis work alongside and also a special thanks to Albert, who was a partner in my project and was always there when I needed to discuss different problems and help in the Lab.

I am also grateful to Dr.Otilia Voigt and Ulf Lamprecht for their time, kindness and for providing me the opportunity to work with them in Department of Radio Oncology at University Hospital of Tübingen, Germany.

Last but not least, I would also like to express my deepest gratitude and love to Soheila. Without her support, I would have hardly been able to pursue my dream in this journey. I will be grateful forever for your love.

Masoud Shafiemehr, Gothenburg, September 2015

Contents

1
Introduction

Based on the estimates of the worldwide incidence and mortality from 26 cancers during the past 30 years, there were 10.9 million new cases, 6.7 million deaths and 24.6 million survivors [1] . Among all the types of cancer, head and neck cancer is in sixth place for the most common cancer worldwide with around 6% of all tumours [2] . Thermal therapy is one of the most common ways that are used for cancer treatment by raising the temperature in the tumor. Thermal therapy can be divided into two types [3]:

- **Hyperthermia (HT),** in the tumor to therapeutic level (40-45°C) for 60 min to induce cell death or to make it more susceptible to the effects of ionizing radiation or chemotherapy. HT treatment is also divided into two types: regional hyperthermia and whole-body hyperthermia.
- **Thermal ablation,** , in this type the temperature off the tumour is above 55°C for 4-6 min. By comparison with HT, it can directly destroy the tumour cells.

During the last decade clinical studies have indicated the ability of microwave HT to dramatically enhance cancer patient survival [54]. However, inadequate heating has lead to disappointing results [38].
Invasive measurements are still considered by many clinicians as the gold standard in monitoring temperature distributions, however it suffers from inadequate information about highly inhomogeneous temperature distributions, for instance in the head and neck region with such geometric complexity and stringent requirements. Magnetic resonance thermometry (MRT) is the most clinically established method for non-invasively temperature monitoring during hyperthermia treatments which provides an accurate 3D temperature image [4]. However, this method has its limitations:

- **Motion artifacts:** its sensitivity to artifacts by the patient movements.
- **Speed:** the low speed of data acquisition.
- **Compatible HT applicators:** a compatible HT applicator is needed since the patient goes inside the MR scanner with the HT applicator and both systems operates simultaneously which can leads to artifacts.
- **Cost:** the price of an MR scanner as well as system maintenance is very expensive.
- **Dimension/Size:** the size of the MR scanner needs a big space to install.

There are other potential non-invasive techniques for thermal monitoring; ultrasound, computed tomography (CT) and microwave thermometry (MWT) [5][6][7].

The present work investigates the feasibility of using microwave imaging to monitor the temperature distribution during hyperthermia cancer therapy.
The scope of this thesis covers the combination of simulations and experimental measurements for both MWT methods to observe the feasibility to perform thermal mapping with microwave tomography (MT) and MRT as the reference method to compare the results with MWT. Also a focus was placed on the design and development of the phantom setup to satisfy the aims of the project.
In Chapter 2, the relevant background in HT treatment, HT treatment planning, image guidance for HT, MRT and MWT are presented. All the simulations and experimental measurements are described in Chapter 3. Chapter 4 presents all results of the data from simulations and measurements, also more explanation about the results are presented and discussed in Chapter 5. Finally, Chapter 6 provides a summary of the work and some future prospects.

2
Background

This chapter details some of the previous studies that have been performed. In Section 2.1, the basics hyperthermia treatment and the various methods used to administer hyperthermia are overviewed. Section 2.2 discusses the importance of using image guidance and different thermal measurement methods. Finally the MRT method and some approaches in MWT are briefly reviewed.

2.1 Microwave hyperthermia

HT has been established clinically as an adjuvant therapy to both radiotherapy and chemotherapy [8]. Microwave HT involves heating the tissue to 40-45°C for 60-90 min [4]. The clinical use of HT was and still is subject to technical limitations and also interdependency between physiology and biology. Therefore, some of the biophysical mechanisms of HT are summarized briefly as follows [9][10]:

Biological effects

- The temperatures beyond 41-42°C have cytotoxic effects on tumour cells.
- A significant increase in sensitivity to heat exposure is observed at approximately 42-44°C.
- The sensitivity of the normal cells to heat is less than tumour cells, for a given cell type.
- The number of damaged cells from radiation and chemotherapy is enhanced at elevated temperatures.

Physiological effects

Normally, in HT treatment there are two different stages. First, for 10-30 min the blood flow to the area often doubles, with no significant cell destruction, and during the second stage blood flow decreases, which is most likely due to localized microthrombosis in the hottest places in the tissue, and the amount of tissue necrosis increases significantly [11]. The physiological responses that can cause important effects to the efficacy of the treatment are noted as follows:

- The temperature distribution in normal tissue is more effective than for cancerous tissue, which is caused in preferred temperature in cancerous tissue and relatively greater therapeutic effect.

- The blood flow is lower in cancerous tissue than in its surrounding normal tissue, therefore the raised temperature will cause a greater blood flow reduction in cancerous tissue.

2.1.1 Combination treatments

There is clinical evidence as well as *in vitro* and animal studies that HT in combination with radiotherapy and/or chemotherapy provides better tumor response for the treatment of high-staged tumors [12].

In ionizing radiation, the therapeutic effect is dependent on the heating temperature and heating time. Typically, in higher temperatures and for longer exposure times a greater effect is seen. In fact, cells in the hypoxic and low-pH areas have more temperature sensitivity. As temperature increases, the blood flow will increase, which results in a higher oxygen concentration in healthy tissue and limit the concentration of oxygen in hypoxic cells in tumor tissue. The maximum radio-sensitivity is obtained during HT treatment, so the best effect is achieved when heat and radiotherapy are delivered simultaneously [12][13].

Another area of interest is to increase the therapeutic effect by combining hyperthermia with chemotherapy. This method can be expressed by the ratio of cell survival at higher temperature with normal temperature for the same drug level in both cases. As studies show, the vascular structure of tumors are disorganized and inefficient which leads to hypoxic regions with poor blood flow in the central part of the tumor, which makes these zones relatively resistant to chemotherapy. As heat decreases, the pH level of extracellular fluid, the cytotoxic effect by the drugs will increase [14].

Although the results are convincing for combination treatments, still more research is needed to improve the therapeutic effect [15][16][17].

2.1.2 HT treatment work flow

The first stage in the HT treatment is to generate the model of the patient by the use of CT and/or MR imaging. The obtained images from CT/MRI are used in hyperthermia treatment planning (HTP). HTP provides important information about the temperature distributions and the complete 3D temperature distribution in the treatment area, which can describe the relation between the heating system, perfusion, discrete vasculature and anatomy [18].

The work-flow for HTP by using head and neck hyperthermia as the treated region is provided in Figure 2.1.

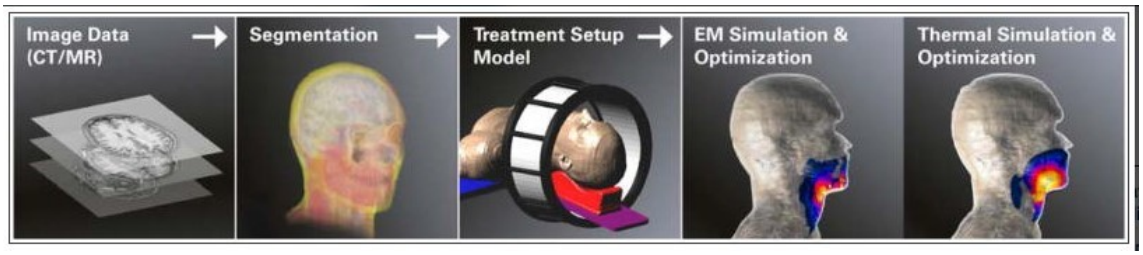

Figure 2.1: The steps required for HTP process [19].

The first step in HTP as Figure 2.1 shows, is obtaining the patient data to establishing a set of treatment parameters with electromagnetic and thermal modeling, which improves treatment quality. Then these data are converted into a 3D model by characterizing the normal and cancer tissue. To generate the 3D model, typical values for electrical, ultrasonic and thermal properties are used. Further, for better accuracy in the treatment planning the geometry and tissue properties (thermal and electromagnetic properties) of the patient must be obtained by segmenting tissues where CT/MRI images use for this [19].
The simulation in HTP is a three-step process [18]:

1. Generate the patient model.
2. Calculate/optimise the distribution power deposited in the tissue
3. Calculate/optimise the temperature distribution in the tissue.

Next is to calculate the specific absorption rate (SAR). As the SAR distribution is calculated and the related pattern established, the resulting temperature distribution in the tissue can be calculated. This step is based on the thermal distribution within the heated region [20]. Then a model of the applicator is added to the patient model to compute the PD and temperature distributions. The next two steps are to optimize the obtained PD and/or thermal distributions. The most important goal in treatment optimization is to ensure the target region receives a high thermal dose and at the same time the healthy tissue absorbs the minimum energy [3]. Calculation of the EM field can be performed by using different solvers such as finite difference time domain (FDTD) and finite elements method (FEM) [21][22]. During the treatment the HT applicator is placed around the patient on the tumour location. The thermometry is also performed during the treatment for further treatment documentation and evaluation. The importance of image guidance is highlighted in this stage.

2.2 Role of image guidance in HT

The first image-guided therapy was a surgery in 1896, in which X-radiography was used to help remove a needle from a woman's hand [23]. This remarkable event took place one year after Roentgen's discovery of X-rays in 1895. This event is important not only because it established the basic profit of x-radiography, but it also improved the result of the surgery (treatment) and introduced a new type of information source. Since then, many techniques and improvements in medical

science have shown that image guidance can be applied in different roles to enhance the treatment.
The role of image guidance for hyperthermia treatment can be divided in four separate roles, and consists of [24]:

1. Pre-treatment determination of the cancer tissue volume.
2. Localization of the hyperthermia applicator or targeting of the heat-delivery source to the cancerous tissue.
3. Real-time monitoring of the delivery of heat energy during the treatment.
4. Post-treatment evaluation of the temperature dose given in the heated tissue.

2.2.1 Thermometry

Knowing and tracking the temperature distribution in the target (tumour tissue) and surrounding tissue may be a way of observing and determining the thermal exposure boundary to improve the HT treatment by protecting healthy tissue from high temperature elevations. Generally, there are two main approaches to temperature monitoring *in vivo* [4]:

- Invasive measurements with interstitial temperature probes, also is known as discrete measurements.
- Non-Invasive Thermometry (NIT) that allows on-line monitoring and control of the quality of the heat treatment.

Invasive (discrete) thermometry was established as a standard method in the last two decades, which can be obtained with EM non-distributing probes. However, the main problem is the invasiveness and the limited information about 3D temperatures due to the spatial resolution of temperature measurements that is limited to the small number of probes [26]. For instance in deep heating in the head and neck region with different biological, electromagnetic and mechanical properties [25]. In addition, the electromagnetic non-distributing probes may lead to artifacts and may perturb the SAR pattern in the heated tissue.
Therefore, the NIT techniques introduced and have been investigated for different modalities; ultrasound, CT and MT are not known as clinical approaches, while NIT by MRI has been used clinically for few decades [4]. In the following sections, all the mentioned techniques for NIT are reviewed.

2.2.1.1 Ultrasound

Ultrasound imaging has been known as a promising modality for temperature measurement for HT treatment since the mid-1970's [27]. There are several temperature dependent properties for ultrasound thermal mapping, which are covered in this section such as velocity of sound, back scattered power and attenuation coefficient [28][29][30]. These acoustic properties are highly dependent on the tissue. For example, the temperature coefficient of the attenuation is around 1-3 % per °C for soft tissue, which for waves at the speed of sound must be ten times higher and this causes difficulties in high density areas such as bone. Also, the thermal coefficient of ultrasound varies with tissue types, which requires calibration before treatment and classification of the tissue [31]. There are also other limitations and technical

challenges have been described in [32], which are the problems to use this method for temperature monitoring during HT treatment.

2.2.1.2 Computed tomography

In the early 1980's CT was introduced as a modality for temperature monitoring. The feasibility of employing a CT scanner to measure the temperature distribution during HT treatment was obtained based on the measurements for the CT-number shift when it is a function of temperature for different materials.
Although temperature mapping by means of CT is considered one of the simplest methods, it is not an interesting modality to investigate because of an extremely low signal-to-noise ratio (SNR) and temperature resolution and consequently requires longer scanning times. Moreover, the patient in CT thermometry will receive additional dose of radiation, which causes problems together with radiotherapy treatment as the patient would receive a high dose [27][33].

2.2.1.3 Microwave thermometry

MT has been an interesting topic for medical applications for many years. It has been investigated in both research and clinical needs for various applications such as cancer and stroke detection [52]. Combining MT and HT as a non-invasive way to thermal imaging during HT treatment has a lower system cost in comparison with other methods like MRT. Also, MWT allows the same antenna system to be used for HT and thermal monitoring. In this method, microwave based thermometry implies temperature mapping consisting of an antenna array to monitor the temperature distribution in the treated region. For the first time, Bolomey et. al [5] showed that MWT is based on the permittivity and conductivity differences for different types of tissues. Later, Miyakawa [34] tried to solve the same problem by using a chirp radar technique, which was not successful for human tissues, since it only works for imaging of low contrast objects. Later a group by Meaney and Paulsen could successfully obtain thermal images that used the Gauss-newton iterative scheme as a reconstruction algorithm in phantoms and in the abdomen of a small piglet [35][36][10].
The Biomedical Electromagnetics Group at Chalmers University of Technology reported results of a feasibility study for microwave based thermometry, which uses an iterative electromagnetic time-domain inversion algorithm for reconstructing the dielectric properties of the object. The algorithm was designed to compare the measured and simulated fields based on FDTD modeling. However, a major limitation with this algorithm is that very long computation times are needed to reconstruct images [37]. Later in this chapter, based on the encouraging results from previous microwave tomographic imaging studies, the accuracy for MWT is investigated and compared with MRT.

2.2.1.4 Magnetic resonance thermometry

MRI based thermometry is known as one of the major technological improvements that was made in the thermal therapy [4]. The temperature sensitivity of MRI and

non-disturbance of measurements at high resolution in MRT are two significant factors in the development of interventional MRI. Since the mid 1980's, MRI has been established as the most viable diagnostic modality for several capabilities such as high-spatial resolution, excellent soft-tissue contrast, sensitivity to blood flow, ability of functional imaging, multi-parametric tissue characterization and multiplanar images [6]. Based on the multi-parametric contrast abilities, MRI meets all roles of image guidance for hyperthermia treatment mentioned in section 2.2. There are three main magnetic resonance (MR) properties, which can be used to monitor the temperature sensitivity and to perform thermal measurements [38]:

1. Spin lattice relaxation time (T_1 relaxation).
2. Self-diffusion coefficient of water.
3. Proton resonance frequency shift (PRFS).

T_1 relaxation

The differences in MR images are described as the image contrast, which for various tissues have different signal intensities or brightness, and form the boundaries between tissues. For the first time, in late the 1980's, Parker suggested an application to construct temperature maps based on the T_1-temperature sensitivity, in the context of HT [39]. Figure 2.2 shows an example of T_1-weighted thermosensitive gradient echo images to monitor thermal-therapy. Different MRI pulse sequences allows us to produce a wide range of contrasts by using and controlling the timing of these sequences.

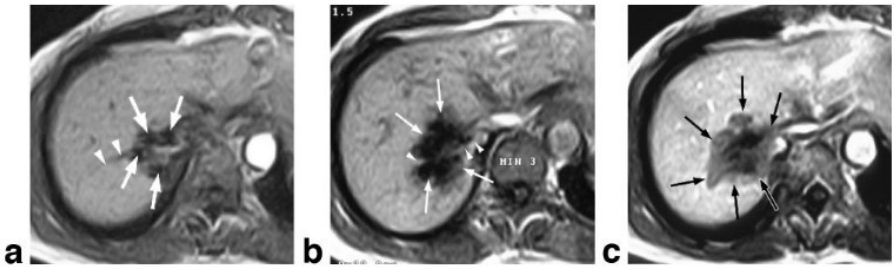

Figure 2.2: MR images of the liver metastases from breast cancer. The T_1-weighted thermosensitive gradient echo sequence is used; (a) shows a clear drop in signal intensity (arrows) in the heated area, (b) a contrast enhanced image obtained immediately after 60 min treatment shows the coagulated area of the tumor tissue, and (c) laser-induced interstitial thermo-therapy T_1-weighted thermosensitive image [7].

T_1-weighted sequences are highly dependent on the type and character of the tissue, therefore they are normally recommended in low-field systems with higher contrasts [38]. T_1 has some limitations in comparison with diffusion measurements (is not technically demanding in terms of fast and strong gradients) and the chemical shift of PRF (less sensitive to the changing and drifting of the PRF in the electromagnet). However, T_1 is applicable in fatty tissue, which is in contrast with the chemical shift of PRF, which is an advantage due to heterogeneous target areas in hyperthermia [40].

Self-diffusion coefficient of water

Another method of MRT is spatial mapping of the diffusion coefficient of water, which was known by LeBihan for the first time in 1989. His experiments showed approximately linear changes of the self-diffusion coefficient in water with temperature by 2.4 % per 1°C [25].

The main problem with using the self-diffusion coefficient of water for thermometry is the fact of restricted diffusion in tissues as the flux rate of the diffusing material is controlled by the permeability of the membrane. In 1992 Cheng and Hernandez [41], found that the restricted diffusion ranges in tissue will increase after a thermal therapy. In their study the tissue showed a less resistive environment for the diffusion of water after treatment. On the contrary, it was realized that the use of long diffusion times in the nuclear magnetic resonance (NMR) experiment (eg. 150 ms) can be effected by this restricted diffusion. But for shorter diffusion times (eg. <30 ms), water molecules cover a shorter distance, which can consequently cause errors in showing changes in the structural resistance of tissue.

Diffusion methods still have some technical and methodical limitations that need further investigation to improve [42].

PRFS-based MRT

One of the most promising methods for MRT compared to those previously discussed, is temperature dependence of the PRF of hydrogen protons. The PRF variation with temperature was observed by Schneider in 1985 and later explored and described by Hindman in 1966 [43][44]. A further description of the physical mechanism of temperature sensitivity of the PRF is given in [27].
When the temperature increases, the hydrogen bonds in water dilate, which increases the magnetic shielding by the water protons by the electrons of the hydrogen bond. The change in the shielding will decrease the resonance frequency of the water protons, which decreases the phase of the water signal. This process is known as PRFS [45]. The advantage of these frequency changes are that they vary linearly with temperature and most tissues have a sensitivity around 0.01 ppm per ° C, based on many experiments in vivo and in vitro. By using gradient echo or offset spin echo sequences the phase sensitive images will be obtained and from that the phase changes can be measured [46]. The following equation defines the signal from these sequences [45],

$$S = A_w e^{-TE/T2^*_w} e^{2\pi i TE(\alpha f \Delta T + \psi))} \tag{2.1}$$

where A_w is the proton density of water, TE is the echo time (ms), the relaxation time (ms) is $T2^*$, the PRFS phase sensitivity (in parts per million per degrees Celsius or ppm/°C) is α, f is the imaging frequency (Hz), ΔT is temperature change (°C) and ψ is the magnetic field offset (Hz).
Figure 2.3 illustrates the determination of the chemical shift difference between the water and N-acetylaspartate (NAA) which was recently used for the validation of high resolution MRT with a new methology for PRFS thermometry [47].

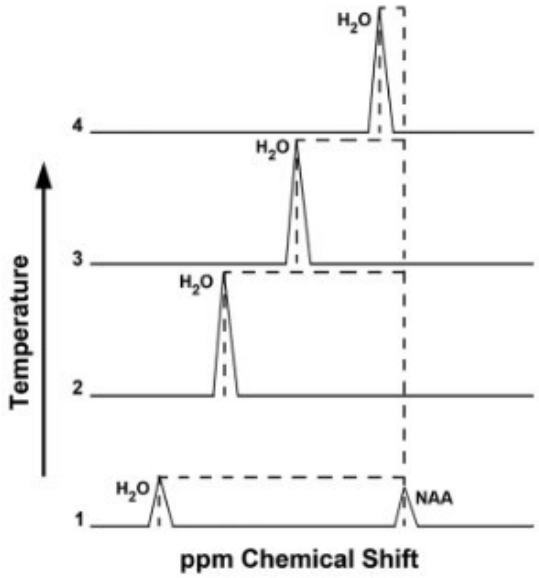

Figure 2.3: Schematic representation of a newly proposed methodology for PRF thermometry: where the NAA reference frequency is obtained from an initial water suppressed spectrum and is followed by a high-temporal-resolution series of non-water-suppressed spectra, measured against the initial NAA reference frequency [47].

A number of studies for different tissue ablations with PRFS techniques such as breast fibroadenomas [48] and brain tissue [49] have been performed. However, using the PRFS method during HT treatment faces some issues not normally observed in thermal ablation. The first challenge is the longer time of an HT treatment than ablation. Typically an HT treatment takes at least 1 hour, which causes magnet instability due to the drift of the main field over time. The second challenge is the determination of the difference of the effective temperature range. Since the temperature for HT treatment is within a small range (41-45°C), the temperature accuracy needs to be better than in ablation where the temperature error is less important since the temperature is much higher than tissue damage level (55-60°C) [50].
Nevertheless, more studies are needed to improve this method to reliably image the extent of the treated region in HT.

3

Materials and methods

The first part of the thesis is focused on the development of a phantom to simulate the neck anatomy, which can satisfy the goals of the thesis in both MRT and MWT. In the second part an antenna array for 3D MT is used (in simulation and experimental setup) to investigate the feasibility of 3D MWT. Also, the developed HT applicator, is simulated to evaluate the system for temperature measurement. Finally, MRT is used to evaluate the temperature accuracy and resolution of the reconstructed MWT images with those of MRT.

3.1 EM fields interaction with the body

3.1.1 Specific absorption rate

To quantify and optimize the temperature distribution, electromagnetic parameters are common to use. The specific absorption rate (SAR) is the for temperature increase in the tissues. SAR is defined as a measure of how much of the transmitted RF energy is absorbed by the human body. The SAR is a function of the electrical conductivity σ, the induced E-field from by the radiated energy and the mass density of the tissue ρ,

$$SAR = \frac{\sigma_{eff}|\overrightarrow{E}|^2}{2\rho}, [W/kg] \tag{3.1}$$

where σ_{eff} is the effective electrical conductivity in [S/m], E is the complex electric field vector and ρ is measured in [Kg/m^3].

3.1.2 Dielectric properties

When the body is exposed to EM fields, different tissues in the body response differently, depending on the tissue properties. Dielectric properties (electrical permittivity ε and conductivity σ) describe the interaction of EM fields with dielectric materials. Permittivity ε is the polarization effect on polarized molecules due to the field, and the conductivity σ depends on the electrical losses in the material due to the currents induced by the field [3].
Figure 3.1 shows the Cole-Cole model by Gabriel et al. [51] and describes the variation of dielectric properties with frequency of developed tissues. As the authors mentioned, the Cole-Cole for dispersive tissues model describes the frequency de-

pendent parameters reliably for frequencies above 1 MHz, therefore it is appropriate for the frequency range of this study (400 MHz to 800 MHz).

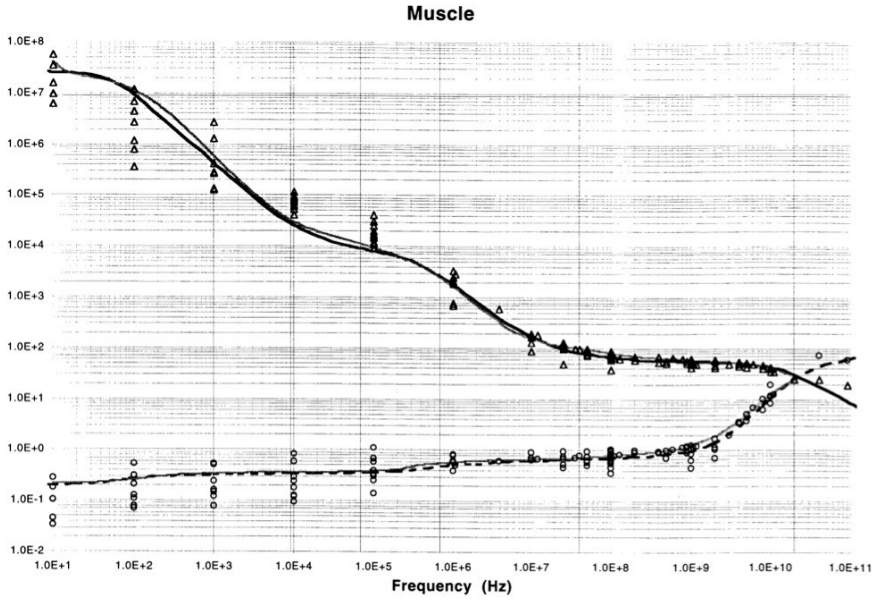

Figure 3.1: Permittivity and conductivity [S/m] of muscle by Gabriel et al., [51] where the black filled and dotted curves are the model prediction, while the grey filled and dashed curves are experimental data at 37 ◦ C and the triangles and circles are data from the literature. Both properties vary with the frequency of the applied field.

3.1.3 Scattering parameters

To characterize a linear microwave system, the scattering matrix is typically utilized. S-parameters describe the electrical behaviour of a linear electrical system, as shown in Figure 3.2.

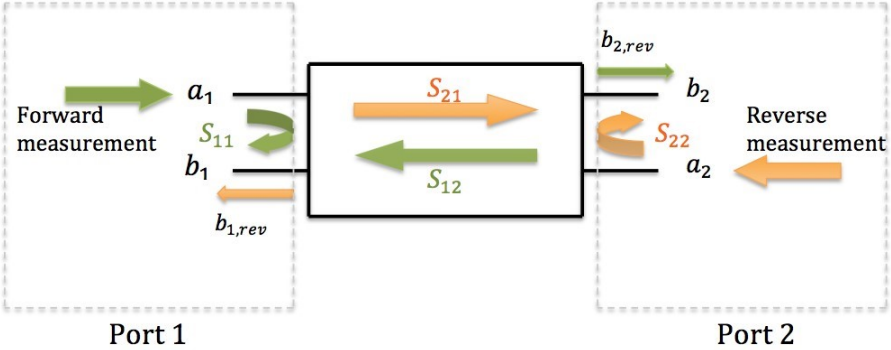

Figure 3.2: The signal flow diagram to illustrate the scattering parameters.

From observing Figure 3.2, the relationship between reflected, incident waves and the scattering matrix is given as follows:

$$\begin{pmatrix} b_1 \\ b_2 \end{pmatrix} = \begin{pmatrix} S_{11} & S_{12} \\ S_{21} & S_{22} \end{pmatrix} \begin{pmatrix} a_1 \\ a_2 \end{pmatrix} \tag{3.2}$$

And expanding the matrices gives:

$$b_1 = S_{11}a_1 + S_{12}a_2 \tag{3.3}$$

$$b_2 = S_{21}a_1 + S_{22}a_2 \tag{3.4}$$

If the given impedance at the load is matched at port 2, then $a_2 = 0$ and b_2 will be totally transmitted. Therefore:

$$S_{11} = \frac{b_1}{a_1} \tag{3.5}$$

$$S_{21} = \frac{b_2}{a_1} \tag{3.6}$$

Also, if port 1 is matched, then $a_1 = 0$, so:

$$S_{12} = \frac{b_1}{a_2} \tag{3.7}$$

$$S_{22} = \frac{b_2}{a_2} \tag{3.8}$$

Where S_{11} is input port voltage reflection coefficient, S_{12} is reverse transmission coefficient, S_{21} is forward transmission coefficient and S_{22} is the output reflection coefficient. S-parameters are typically measured with a vector network analyser (VNA) as described in section MWT.

3.2 Phantom design

In order to compare MWT and MRT, the tissue-mimicking phantom was developed. The agar phantom composed of water (570 ml), agar (30 ml), salt (7 ml) and sugar (400 gr) for a one liter phantom. The cylindrical phantom with diameter 150 mm and length 400 mm contains silicone tubes of various diameters placed along the phantom (35, 30, 12, 8 and 6 mm). The water circulation inside the tubes simulate the heating action, as a high accuracy in of both methods needs a homogeneous temperature distribution along the phantom. The developed phantom rig for three wall thicknesses (1 mm, 3 mm and 5 mm) were simulated and the effects of the (silicone) tube on E-fields was evaluated as shown in Figure 3.3.

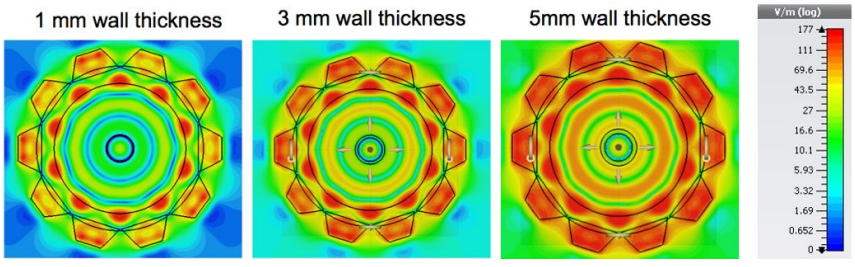

Figure 3.3: The effects of tube wall thickness on E-field in f = 800 MHz.

Also, the amplitude differences of S_{11} for various wall thicknesses are shown in Figure 3.4.

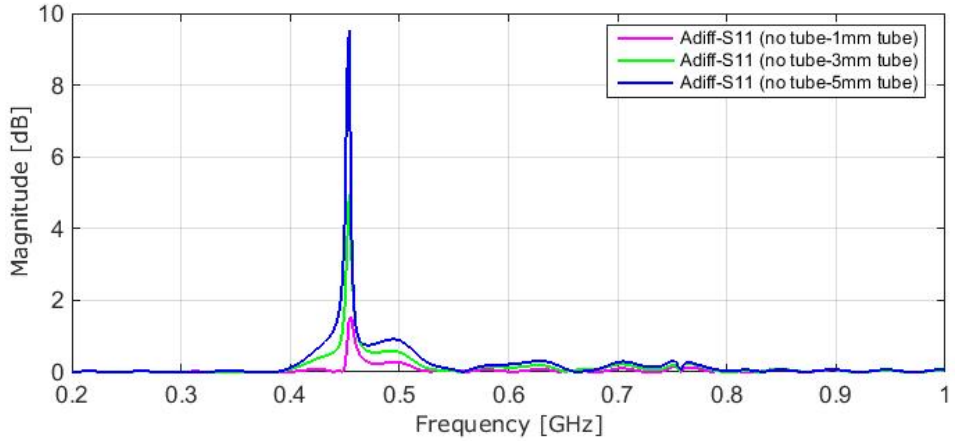

Figure 3.4: S_{11} amplitude differences for various wall thicknesses.

The tube with 1 mm wall thickness shows the amplitude difference less than 2 dB while for 5 mm case the difference reach 10 dB. Therefore the thinnest tubes available on the market were used. Figure 3.5 shows the final design with silicone tubes of various diameters placed in the phantom.

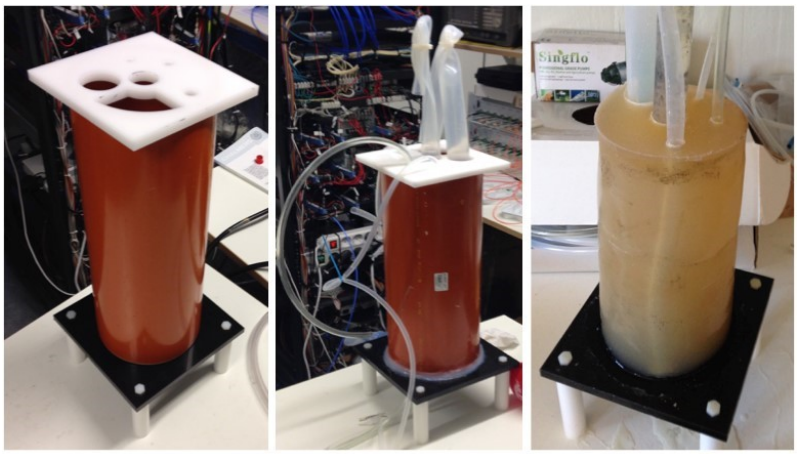

Figure 3.5: Photographs of the designed phantom; (a) the phantom rig consisting of three parts, (b) various tube sizes with 1mm wall placed in the phantom rig and (3) tissue mimicking phantom, with the outer cylinder removed.

The phantom rig contains three main parts: top plate, bottom plate and a cylinder as the main body, which were designed in SOLIDWORKS and manufactured. Figure 3.6 shows how the tubes fix into the bottom plate and the phantom inside the cylinder. To avoid any leakage after pouring the hot phantom in the cylinder, all the tubes were glued with silicone glue to the bottom plate.

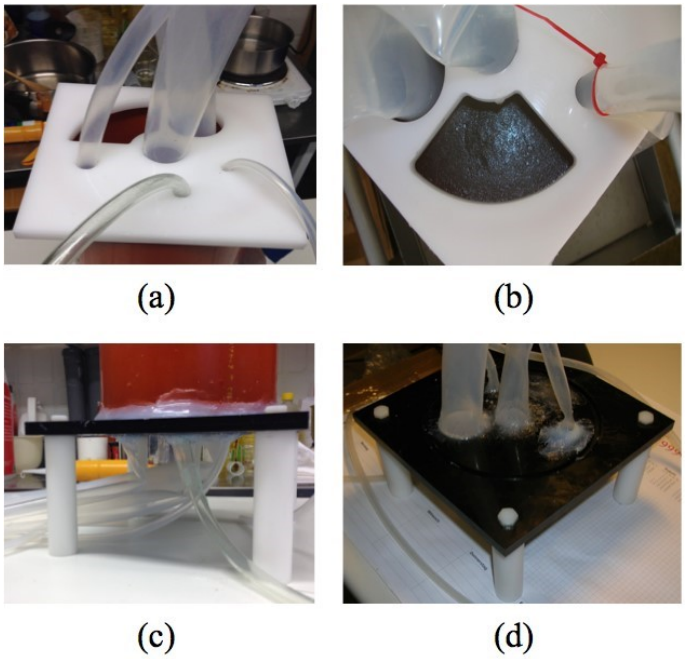

Figure 3.6: Photographs of the placement of used tubes shows; (a) top plate with silicone tubes, (b) the big hole on top plate used to pour the phantom inside the cylinder, (c) bottom plate containing 4 feet and tubes are also placed at the other side, and (d) silicone glue was used to fix tubes to each hole on the bottom plate.

A water pump together with a temperature regulator was used to heat and circulate the water through the tubes. Therefore, tubes were connected to the pump at both sides as input (top plate) and output (bottom plate).

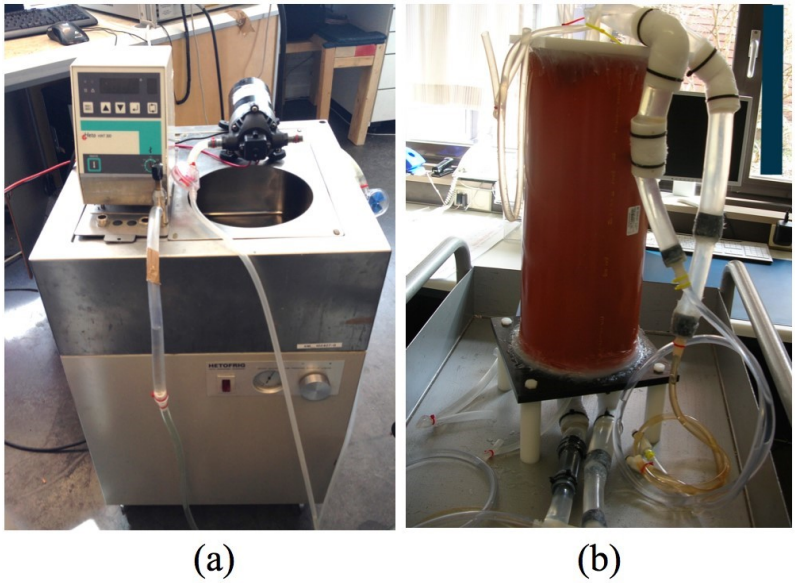

Figure 3.7: Photographs of the water circulation setup; (a) The pump and the temperature regulator, (b) prepared phantom with long tubes at input and output to connect to the pump.

3.2.1 Temperature stability

The temperature stability inside the tubes was evaluated in order to determine whether the temperature is homogeneous along the phantom. The relative measurement were performed in two steps:

1. The temperature stability along the tube at the input and output while water was circulating,
2. The temperature stability inside the tube when the water circulation was stopped.

Water was heated to temperatures 25, 30, 35 and 40°C and circulated by the pump, while two fiber-optic probes placed inside the tube, measured the temperature at the input (close to the top plate, Channel 1) and at the output (close to the bottom plate, Channel 2). Each probe contained 8 thermal sensors with 1 mm distance between each sensor.

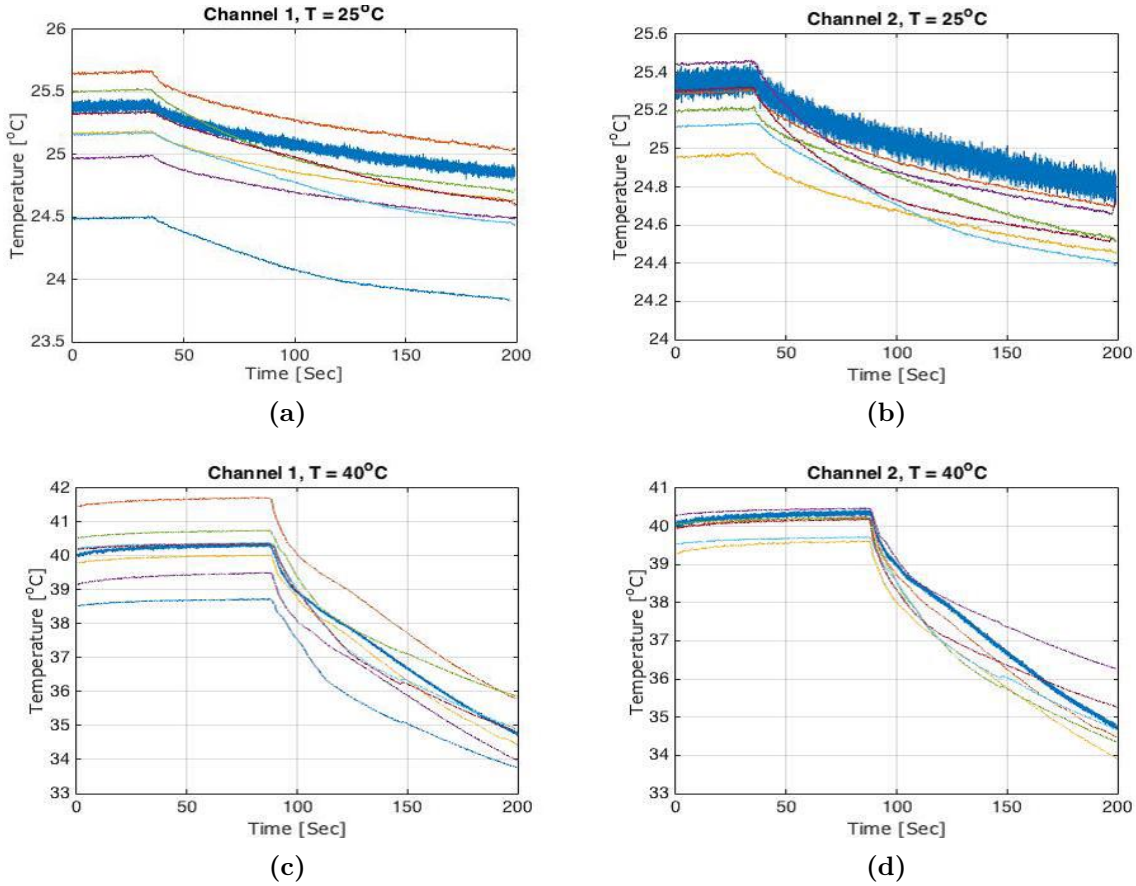

Figure 3.8: Temperature stability along the tube, measured in real time.

Figure 3.8 shows the measured temperatures for 25 and 40°C warm water. The water was circulated for 90 s while sensors were measuring the temperature, then the circulation was stopped while the temperature changes were measured. The highest measured temperature in Figure 3.8a is 25.5°C during the water circulation, while in the same probe for another sensor it shows 24.5°C. Also, in Figure 3.8b

the highest and lowest recorded values are 25.4 and 25°C respectively. Figure 3.8c and 3.8d are for the same condition while the the temperature of the circulating water was 40°C. The temperature difference between each sensors in one probe and also between two probes, provided the homogeneity inside the tube, while water was circulating.
The second part of the experiment was to measure the temperature stability inside the tube while the there was no water circulation and the warm water remain inside the tube while the probes were measuring the temperature. For water temperature T = 25°C (Figure 3.8a and 3.8b), after 150 s there was around 1°C reduce in the temperature, while for T = 45°C (Figure 3.8c and 3.8d) the temperature reduced around 3°C.

3.3 Microwave thermometry

MWT was evaluated in two different antenna systems as is shown in Figure 3.9:

1. MW tomography system consisting 24 monopole antennas in 3 rings.
2. Neck HT applicator consisting 10 bow-tie antennas.

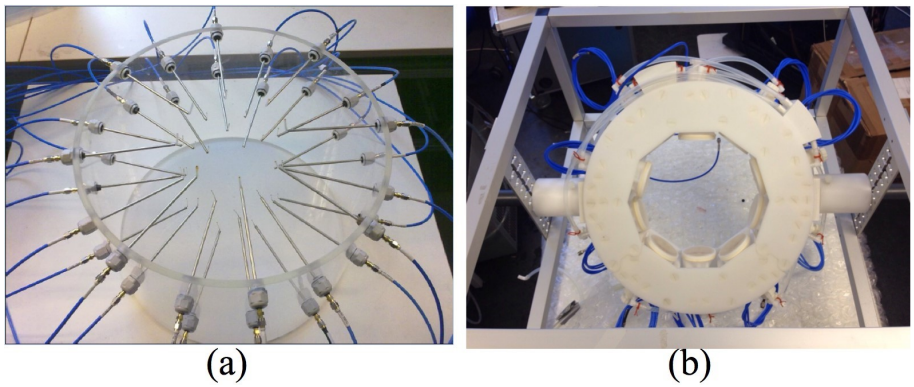

Figure 3.9: Two different antenna systems used for MW-thermometry; (a) the 3D antenna array with 24 monopole antennas and (b) HT applicator with 10 Bow-tie antennas.

Both simulations and measurements were performed for evaluation. The simulated setup was used to (i) compare the results with the laboratory experiment measurements and (ii) reconstruct the 3D thermal image.

3.3.1 MWT with tomography (monopole) system

a) Simulation
Figure 3.10 presents the developed phantom setup and the microwave tomography 3D antenna array, which were simulated together in CST STUDIO 2014. The material of the tank with antenna arrays was modeled as Plexi glass and the inside of the tank was modeled as water and served as a matching liquid. The simulation is performed for four tubes (6mm, 12mm, 30mm and 35mm) filled with muscle phantom material.

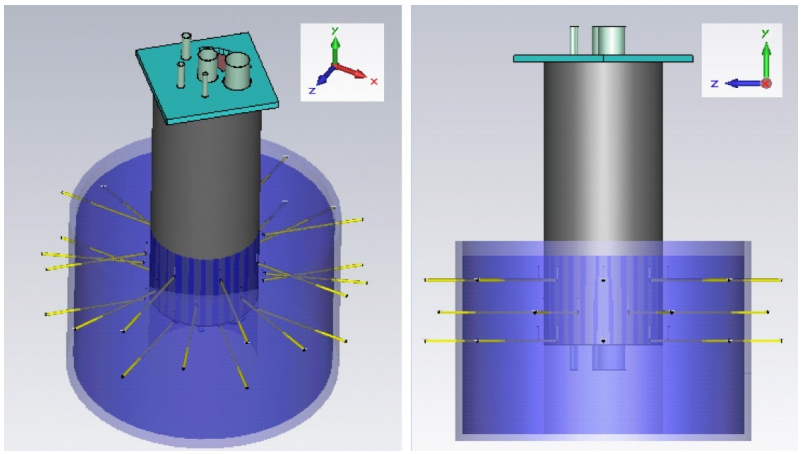

Figure 3.10: CST model of the whole setup; front view (right image) and perspective view (left image).

Due to the long simulation time for each antenna (4 hours), only 2 rings (the middle and top rings) consisting of 16 monopole antennas out of 24 were simulated. Each of the 16 antennas were used as a transmitter and excited one by one, to obtain a 16 $\times$ 16 scattering matrix. The simulations were performed for each tube for different muscle phantom temperatures (20, 25, 30 and 35°C) inside that tube.

Also, a single monopole antenna was simulated separately to characterize the antenna. Figure 3.11 shows the single antenna model in CST:

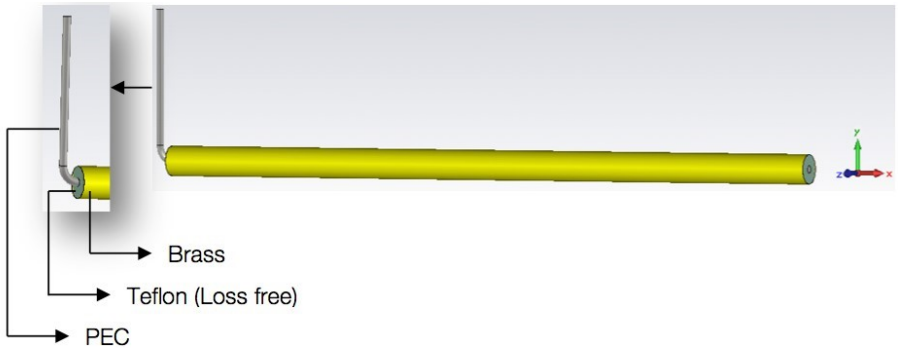

Figure 3.11: CST model of a single monopole antenna.

To reduce the time that was needed for simulation, the model of the antenna has been simplified, where a discrete port with impedance Z = 50Ω was connected between the outer layer (brass) and the core (PEC), instead of the feeding coaxial cable and matching network.

b) Measurement setup

The experimental setup used in the lab is shown in Figure 3.12. Figure 3.12b shows the phantom placed inside the 3D microwave antenna array. All the 24-monopole antennas are connected to the switching matrix that is connected to the VNA.

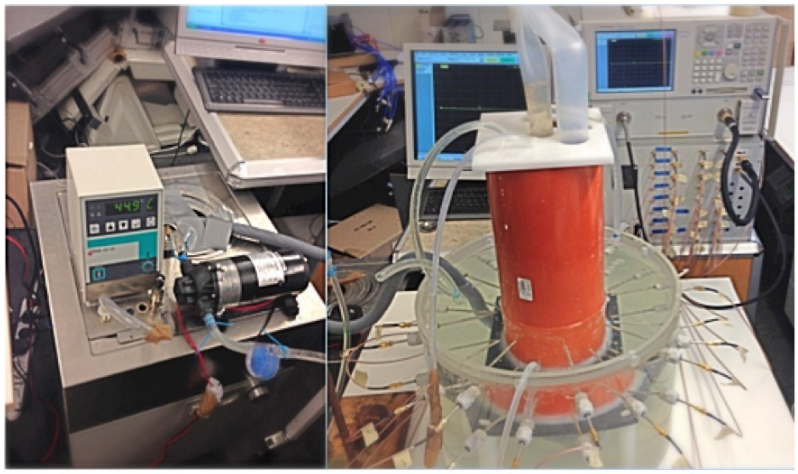

(a) (b)

Figure 3.12: The complete setup for measurement with antenna array.

Figure 3.12a shows the pump and the connected temperature regulator. Liquid phantom was circulating through the selected tube with a constant flow rate, while all other tubes were filled with stationary liquid phantom. In the measurement four tube sizes (6, 12, 30 and 35 mm in diameter) were used as in the simulation to generate the scattering matrix for each tube for different temperatures of liquid phantom (20, 25, 30, 35, 40 and 45°C). Smaller steps for a finer temperature resolution were investigated for every 1°C in the range of 20-30°C for all tubes. The measurement for each setup was performed twice, to ensure the stability of the measured S-parameters.

3.3.2 MWT with HT applicator

One of the biggest advantages of MWT is the potential use of the same antenna array for both heating and thermal monitoring. Therefore, the analogous data were obtained with the newly developed HT applicator aimed for treating a tumour in the neck region. Originally, the system consisted of 10 self-grounded bow-tie antennas arranged in a ring as shown in Figure 3.13.

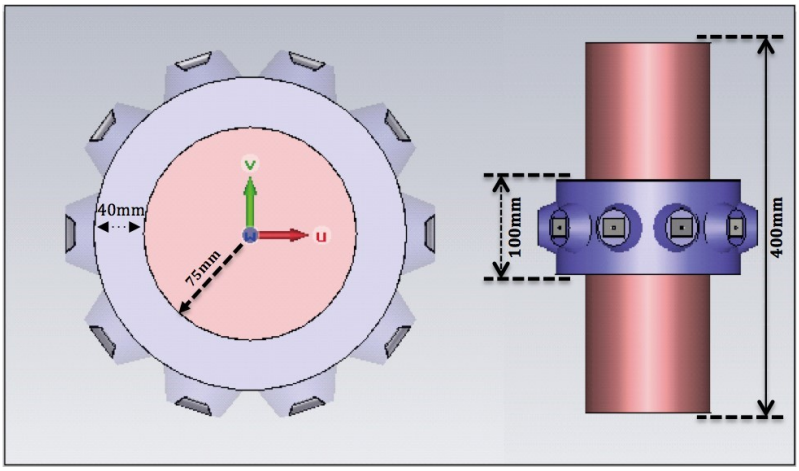

Figure 3.13: Top and front view of the one-ring applicator using 10 antennas.

Between the antenna ring and the surface of the phantom a water-bolus is placed to [55]:

1. cool down the phantom surface (patient's skin) to protect from overheating.
2. improve impedance matching between the body and the antenna applicator.

Since the optimal thickness of the water bolus is around 20 mm, the applicator was adapted to a setup with two rings of 5 antennas. The applicator diameter was thus reduced for a smaller neck.

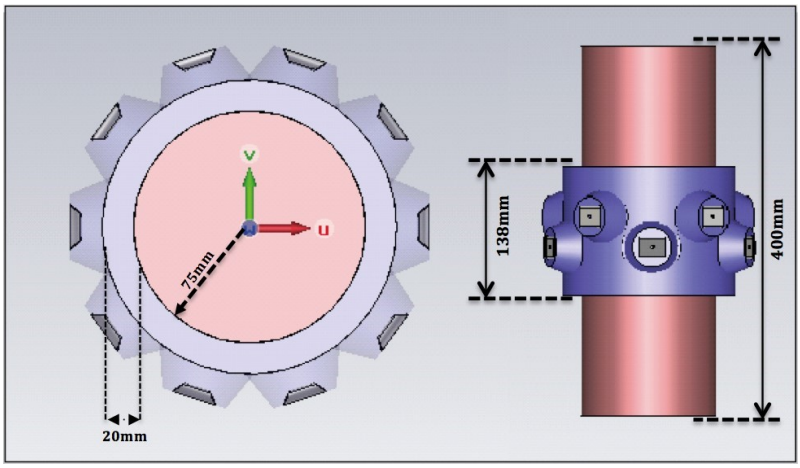

Figure 3.14: Top and front view of the two rings applicator by 10 antennas.

Figure 3.15 shows the single antenna model in CST, where a discrete port with impedance Z = 30Ω was used instead of simulating the feeding coaxial cable and switching network as well.

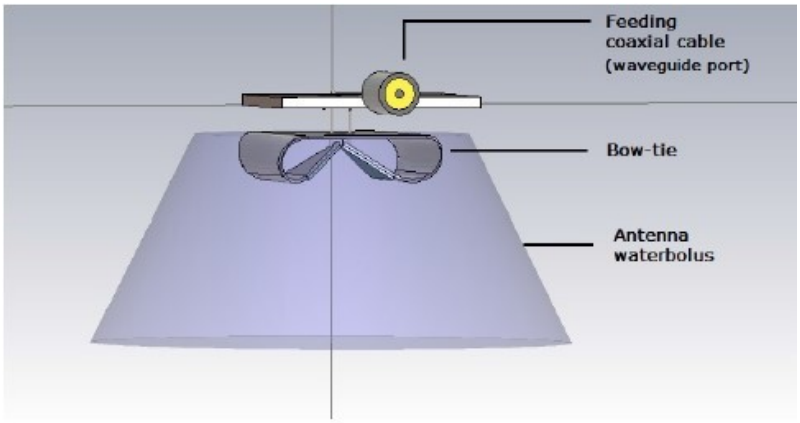

Figure 3.15: The bow-tie microwave antenna [55].

Figure 3.16 shows schematics of the HT and MT systems for thermometry. In both systems the central tube (ϕ = 30mm and 1mm wall thickness) was in the line of sight between two antennas indicated by red arrows. For the HT applicator antenna 1 and for the MT system antenna 3 were used for transmission, while antenna 6 and antenna 7 were chosen as receiver antennas respectively.

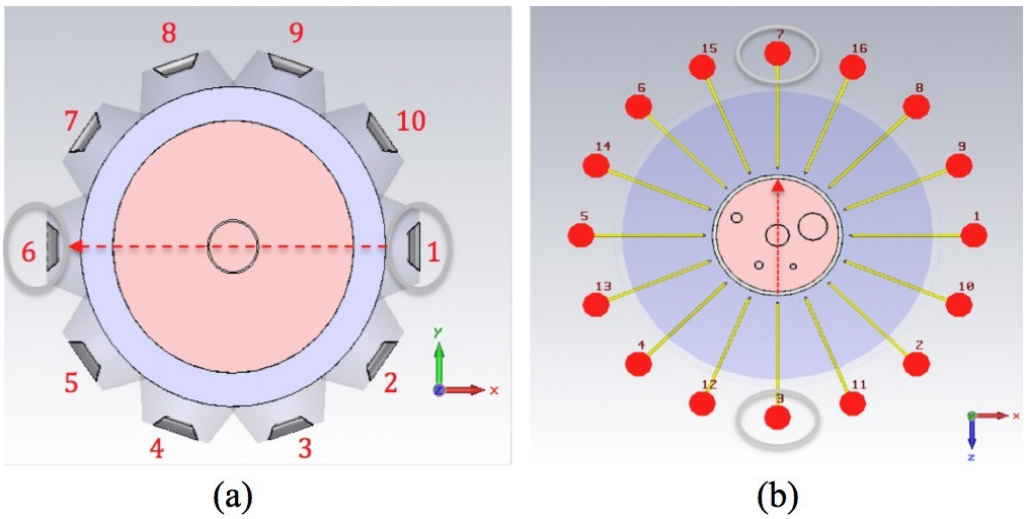

Figure 3.16: The CST model of (a) the microwave HT system, (b) the microwave tomography system.

3.3.3 Effect of temperature changes on scattering data

The effects of temperature changes on scattering data for muscle phantom at different temperatures were evaluated. In the simulation, the scattering data were obtained first for the phantom before the temperature was increased at the center (Figure 3.17a) and then scattering data were obtained when the temperature was elevated to 25, 30, 35, 40 and 45°C, inside the 30 mm tube in diameter and wall thickness of 1 mm (Figure 3.17b).

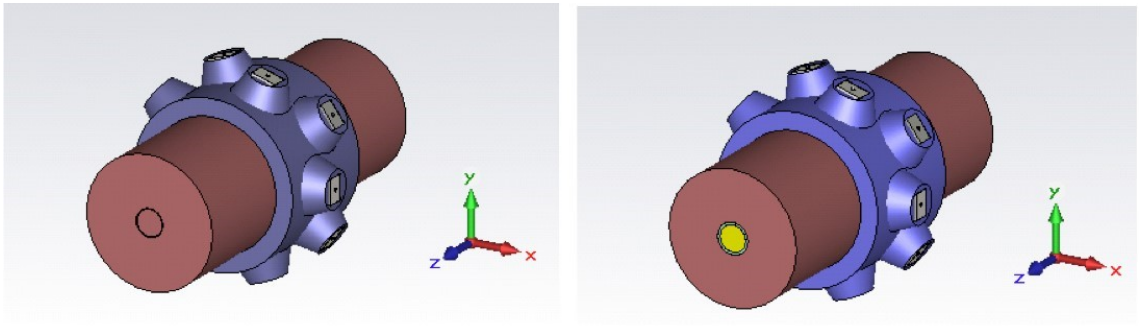

Figure 3.17: The simulated muscle phantom with the new HT applicator; (a) before temperature change and (b) after the temperature was increased at the center, which the colour yellow indicated elevated temperature.

Based on the previous study in [57], the dielectric properties (permittivity and conductivity) of the muscle tissue are varied for different temperatures at different frequency points. In Appendix A, the values used for permittivity and conductivity corresponding to each temperature in the simulation are given.

3.3.4 MW-thermometry evaluation

The obtained data were evaluated both quantitatively by means of data and qualitatively by obtaining thermal maps.

a) Good Data Ratio

The amount of obtained data in the simulation and lab experiment depends on the number of antennas (combination of transmitter receiver pairs), and the frequency points that can be used for the measurement. Since a microwave measurement generates a large set of data, it is important to know the good data.
The s-parameters were measured first for the system at room temperature before the temperature was increased for the liquid muscle phantom inside the tubes and then s-parameters were measured when temperature elevated to 25, 30, 35, 40, 45°C. For the scattering measurements that have been made before any heating, it is denoted S_{klm}^{ref} (the reference data) and the same measurement has been made after heating, which is denoted as S_{klm}^{heat}, where K is the number of transmitting antennas, L is the number of receiving antennas and M is the number of frequency points and the good data from the scattering data can be calculated as follows [52].
The difference in amplitude and phase of the scattering parameters were calculated as:

$$A_{klm}^{diff} = 20log_{10}\left|S_{klm}^{heat}\right| - 20log_{10}\left|S_{klm}^{ref}\right| \tag{3.9}$$

$$\theta_{klm}^{diff} = \angle S_{klm}^{heat} - \angle S_{klm}^{ref} \tag{3.10}$$

The measurement accuracy of the system was defined by the amplitude error in dB, A_{dB}^{error}, and phase error, θ^{error}. The scattering data from the reference measurement and after heating must fit in at least one of these conditions:

$$A_{klm}^{diff} > A_{dB}^{reeor} \tag{3.11}$$

$$\theta_{klm}^{diff} > \theta^{error} \tag{3.12}$$

Another condition is also considered; the measured data must be above the noise floor of the system. The noise floor is denoted in terms of its amplitude in dB, A_{dB}^{floor}. Hence, the scattering data from the reference system and that after heating are detectable if:

$$20log_{10}\left|S_{klm}^{ref}\right| > A_{dB}^{floor} \tag{3.13}$$

$$20log_{10}\left|S_{klm}^{heat}\right| > A_{dB}^{floor} \tag{3.14}$$

To derive the final relations for the GDR, Eq. (3.9) to (3.14) are combined and the following four relations are obtained:

$$A_{klm} = \begin{cases} 1, & if\ A_{klm}^{diff} > A_{dB}^{error} \\ 0 & Otherwise \end{cases} \tag{3.15}$$

$$T_{klm} = \begin{cases} 1, & if\ \theta_{klm}^{diff} > \theta^{error} \\ 0 & Otherwise \end{cases} \tag{3.16}$$

$$B_{klm} = \begin{cases} 1, & if\ 20log_{10}\left|S_{klm}^{heat}\right| > A_{dB}^{floor} \\ 0 & Otherwise \end{cases} \tag{3.17}$$

$$C_{klm} = \begin{cases} 1, & if\ 20log_{10}\left|S_{klm}^{ref}\right| > A_{dB}^{floor} \\ 0 & Otherwise \end{cases} \tag{3.18}$$

From the given equations it can be concluded that the GDR is the ratio between the number of good data and the total number of data when the measured data are above the noise floor of the system and the scattering parameters have a larger change than the system error. The definition of the GDR of the system is obtained for the amplitude and phase system error separately, also for the amplitude and phase when both are above the system error.
The three following equations are used to generate the GDR:

Good amplitude data ratio

$$\Upsilon_{GDR(A_{klm})} = \frac{\sum_{klm} A_{klm} \cap B_{klm} \cap C_{klm}}{KLM} \tag{3.19}$$

Good phase data ratio

$$\Upsilon_{GDR(T_{klm})} = \frac{\sum_{klm} T_{klm} \cap B_{klm} \cap C_{klm}}{KLM} \tag{3.20}$$

Good data ratio

$$\Upsilon_{GDR} = \frac{\sum_{klm} (A_{klm} \cup T_{klm}) \cap B_{klm} \cap C_{klm}}{KLM} \tag{3.21}$$

In the notation above $\cup$ denotes element-wise **or**-operations, and $\cap$ denotes element wise **and**.

b) Fast 3D image reconstruction

Among the existing techniques for MW imaging, most of them are very time consuming and require extensive computing resources. Therefore, in the previous study [53], a fast 2D image reconstruction algorithm was developed and in this work it is modified for 3D.
In this algorithm the difference in dielectric properties of the phantom are estimated from the change of the EM field (the data that are directly measured by the antennas propagation inside the tubes). The simulation and measurement results were used in the algorithm to calculate the conductivity and permittivity of the muscle phantom. Based on the previous studies, the inverse scattering equation (Eq. (3.22)), is the mathematical way that can describe the relationship between the change of the scattering EM field and the change of the dielectric properties in this field.

$$\delta E_s^{tot}(\overrightarrow{r})) = (\frac{2\pi f}{c_0})^2 \int G(\overrightarrow{r} - \overrightarrow{r'}) E_0(\overrightarrow{r'}) \delta\varepsilon(\overrightarrow{r'}) \overrightarrow{dr'} \tag{3.22}$$

where f is the frequency and c_0 is the speed of light in vacuum and $\delta E_s^{tot}(\overrightarrow{r}))$ denotes the differences between the electromagnetic fields for the simulation and measurement in each receiving antenna. On the right side of the equation, $E_0(\overrightarrow{r'})$ is the estimated electric field (generated by the FDTD simulation) in the imaging domain when the nth antenna is transmitting a signal for the reference temperature and $G(\overrightarrow{r} - \overrightarrow{r'})$ is the estimated electric field in the imaging domain when the corresponding receiving antenna is used to transmit the signal. Finally, $\delta\varepsilon$, the deviation of dielectric properties from Eq. (3.22) is obtained by running the algorithm [53].
The reconstructed images were generated by using E-field from simulations for the reference temperature (T = 20°C) and the S-parameters for reference temperature and heated temperatures (T = 25, 30 35°C). The simulation were performed for frequencies of; 400, 500, 600, 700, 800, 900, 1000, 1200 and 1400 MHz.

3.4 MR-thermometry measurement

The MR experimental setup is analogous to the MW setup. The heated spot is represented by circulating heated water (instead of liquid phantom) through the tubes at different temperatures while the phantom is located inside the MR scanner. Two setups for the MR scanner are applied; the phantom placed on the MR table

under the MR body coil, and the phantom placed on the MR table under the MR head coil. The laser on the MR scanner was positioned in the middle of the phantom (18.5 cm from the bottom plate of the phantom) and the direction of water circulating through the tube was from the MR-bore towards the thermal mapping box of the hyperthermia system (feet (MR) ⇒ head (MR)).

The measurements were performed for three size of tubes (ϕ = 35, 30 and 12 mm), and the circulated water was heated to seven different temperatures (20, 23, 25, 28, 30, 33 and 35°C). All the experimental measurements for MRT were done with a Siemens 1.5 Tesla MR scanner at the University-Clinic of Tübingen in Germany. Figure 3.18 shows the complete experimental setup with the phantom positioned horizontally on the slide table of the MR scanner. For the MR data acquisition system a 1.5 Tesla MR scanner (Siemens AG, Erlangen, Germany) was used; the processing of MR data to map MR temperatures was done by the Sigma Hyper Plan Viewer, a thermometry system for temperature-control with Bowman thermistors (BSD Medical Corp.).

Figure 3.18: The complete setup for measurement with body coil MR scanner. Phantom setup with MR scanner on the left and the water pump and temperature regulator on the right.

The water pump and temperature regulator were placed outside the MR room to avoid artifacts. Therefore, the tubes (already located inside the phantom for water circulation), were connected to the long tubes (4 m each for input and output), which were connected to the water pump outside the room.

The reference temperatures were measured with two temperature probes with an accuracy of ±0.1°C. Originally, the probes were located between the central water tube (ϕ = 30 mm) and the muscle phantom as shown in Figure 3.19b. The second probe was fixed outside the same water tube, due to the tube wall thickness (1 mm).

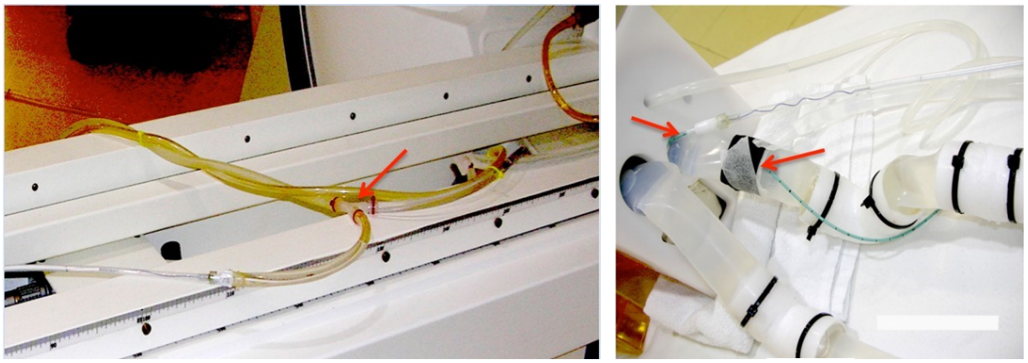

(a) (b)

Figure 3.19: Positioning of (a) one Bowman temperature probe placed inside the water tube and (b) the two Bowman temperature probes outside the water tube.

Since the observed temperatures did not correspond to the temperature set on the water pump. Therefore, one probe was inserted inside the water tube through a T-shape connector (3.19a). With the new position for the probe, the temperature of the circulated water inside the tube was showing the temperatures set in the pump.

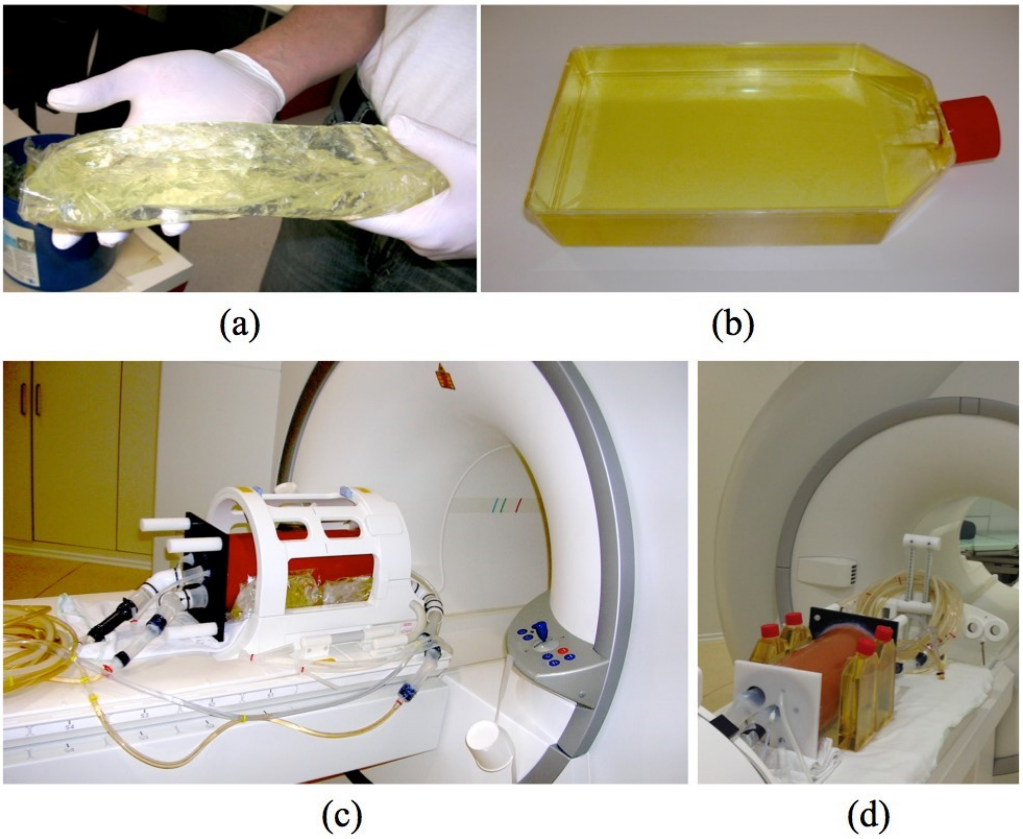

(a) (b)

(c) (d)

Figure 3.20: (a) Oil bag for MR drift correction, (b) oil bottle for MR drift correction, (c) phantom with oil bags positioned on the MR table under the MR head coil and (d) oil bottles placed on both sides of the phantom for the MR body coil.

Water circulation during the MR acquisition causes a phase drift in the acquired signal. In order to correct this phase drift, which also causes a reduction of signal-to-noise ratio (SNR) and also for increase the B_0 field homogeneity, oil were used. As Figure 3.20d shows, four oil bottles (17 cm height, 12 cm width) for the measurement with MR body coil were used, whereas for the measurement with the MR head coil, four oil bags were used.

3.4.1 Data acquisition and processing

The first step before data acquisition is the phantom registration in the MR-computer. Since the phantom was non moved between acquisitions, the phantom was localized only once at the very beginning (Figure 3.21). The MR images use the magnitudes and phases in sequences. The temperature-sensitive images were acquired with gradient-echo (GRE) with a resolution typical of: TE1 = 4.76 ms, TE2 = 19.1 ms, TR = 600 ms, 25 slices in 10 mm distances, 256 × 256 matrix, single measurement. The acquisition time was 100 s. The magnitude data sets (T_1-weighted) are used for checking the correct position and a reasonable SNR.

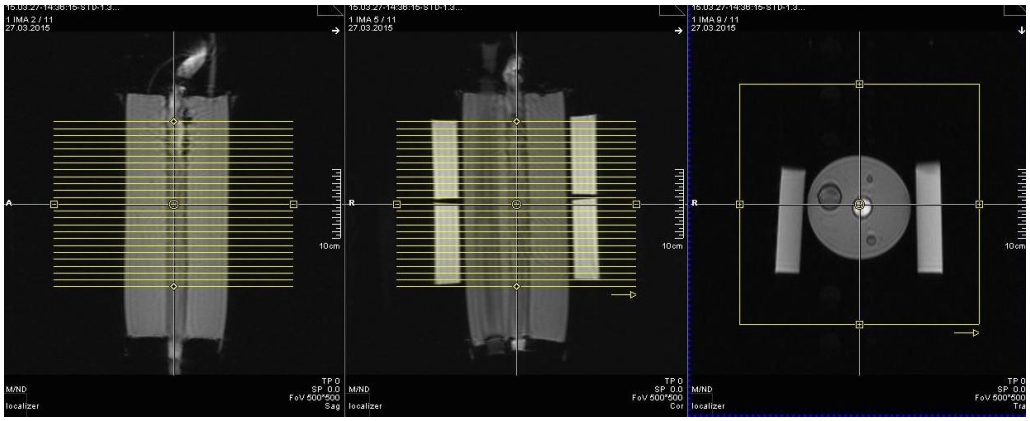

Figure 3.21: The image of the phantom registration data with the body coil.

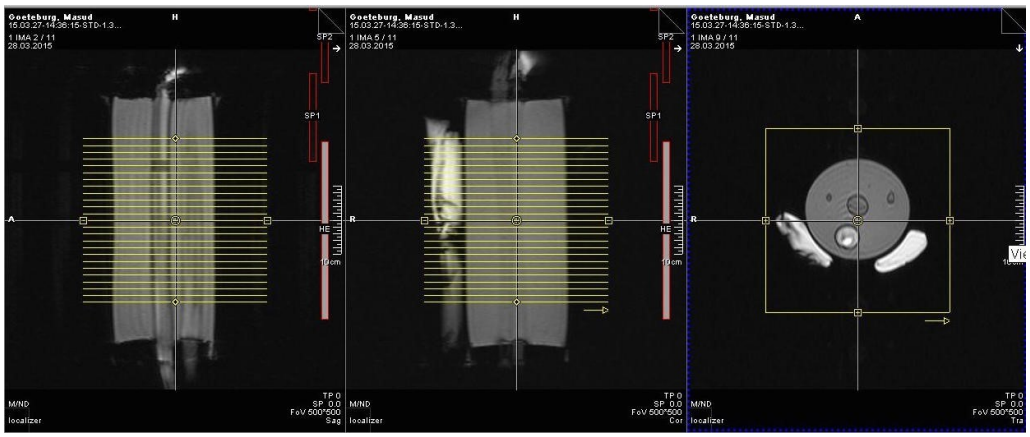

Figure 3.22: The image of the phantom registration data with the head coil.

All these MR data are transferred to the other personal computer for further processing with the software platform Sigma Hyper Plan Viewer (SHPV) [54]. The MR temperature images are calculated in this software (PRFS method) and the corresponding temperature image is generated.

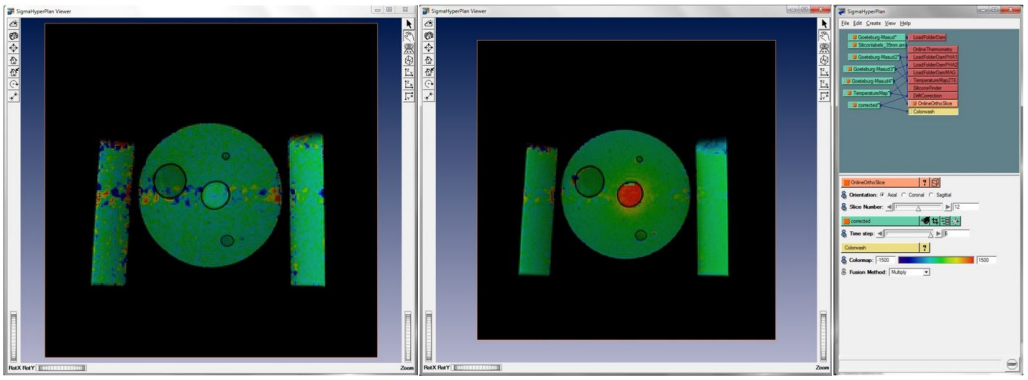

Figure 3.23: The temperature images from SHPV with the body coil; 20°C water circulated through the central tube (left), 33°C water circulated through the central tube (right).

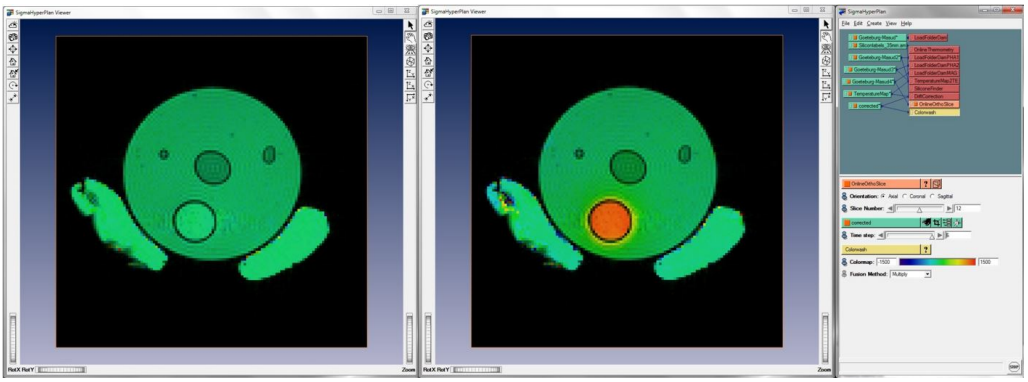

Figure 3.24: The temperature images from SHPV for head coil; 20°C water is circulated through the biggest tube on the side (left), 33°C water is circulated through the biggest tube on the side (right).

Figure 3.23 and 3.24 show one slice (same slice in all) of the acquired MR data with the body coil and head coil respectively, which are processed in SHPV. The temperature difference can clearly be seen between these images.

3.4.2 Data evaluation

In order to evaluate the resolution of MRT, the measured raw-data were analyzed in MATLAB. In the PRFS method, the temperature change (ΔT) is calculated as [45]:

$$\Delta T = \frac{\Delta \phi}{\gamma \alpha B_0 T E} \tag{3.23}$$

where $\Delta\phi$ is the difference between the phase of the image at one echo time (acquired before and after temperature change), γ is the gyromagnetic ratio of a proton (42.58 MHz/Tesla), B_0 is the main magnetic field strength (1.5 Tesla), TE is the echo time in millisecond, and α denotes the PRFS thermal coefficient (the PRF change per degree Celsius).
The α-parameter is MR specific and can greatly effect the accuracy of the temperature change calculation. In other words, an incorrect α value leads to an inaccurate temperature distribution, which would have serious consequences in a clinical treatment. Therefore, a calibration of the α-parameter was performed. Eq. 3.23 is applied to subtract images that are calculated from the phase differences $\Delta\phi = \phi_{ref} - \phi_{heat}$ (for each pixel in a 256×256 matrix). By this process a large set of values for α-parameter are obtained. The accurate α value can be calculated as a function of real temperature (set on water pump) and $\Delta\phi$ of each pixel.

4

Results

This chapter consists of two parts: MWT results (Section 4.1) and MRT results (Section 4.2). In Section 4.1 results evaluating the measured GDR values for the MW tomography system (experimental measurements and simulation) and HT applicator (only simulation). Also, the reconstructed MW images for the 3D MW tomography system are shown. The results of S11 and SAR for the old and new HT applicators are presented and also the effect of temperature changes on the transmission coefficient are evaluated.

4.1 MW-thermometry results

The results for reflection and transmission coefficients of the HT and MT systems for thermometry are plotted in Figure 4.1. In Figure 4.1a, the transmission coefficient for the MT system for lower frequencies in the range of 0.4 to 0.8 GHz goes down to -60 dB, while for HT applicator it reaches -25 dB. Also, for frequencies above 1 GHz HT applicator the transmission coefficient is around -50 dB while for MT system it reaches -80 dB.

Figure 4.1b shows that the reflection coefficient for the HT applicator is -10 dB in the frequency range of 0.5 to 0.8 GHz, while for MT system reaches only -5 dB.

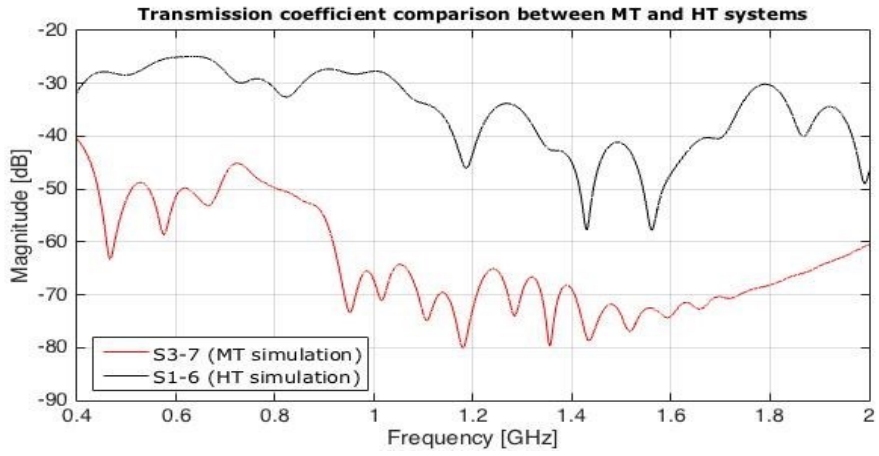

(a)

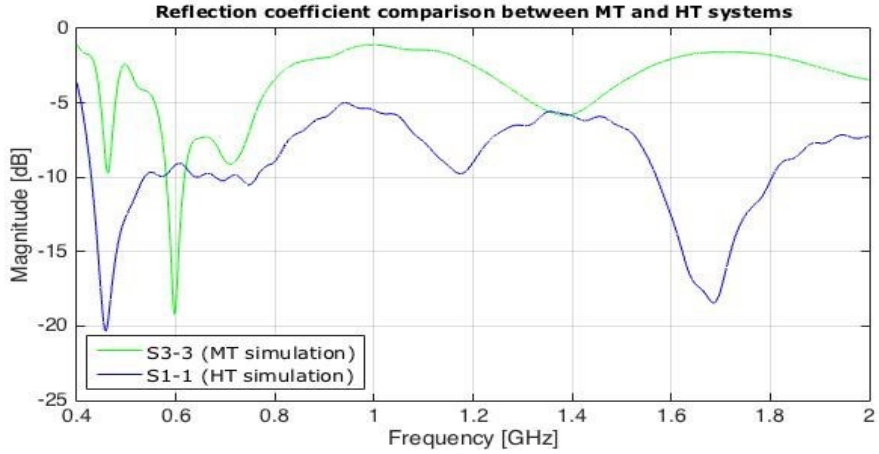

(b)

Figure 4.1: The (a) transmission coefficients and (b) reflection coefficient between 2 antenna combinations for the HT and MT systems.

4.1.1 MWT with tomography (monopole) system

a) GDR results from simulation

Figure 4.2 shows the calculated GDR using Eq. (3.19) for the simulated MW tomography system. In the current result 16 antennas were used in the simulation while the temperature differences were 25-35°C.

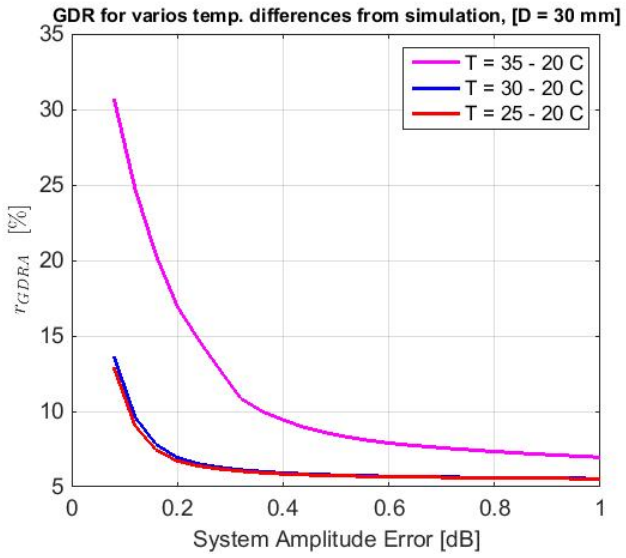

Figure 4.2: The GDR% as a function of the system amplitude error for the MT simulation setup.

In the calculation the amplitude noise floor was $A_{dB}^{floor} = -80$ dB, and the results were plotted as a function of the system amplitude error A_{db}^{error} and the phase error, $\theta^{error} < 1$ deg. The highest GDR value is 30 % obtained for the largest measured temperature difference ($\Delta T = 15$°C). Whereas, for the other two measured temperature differences, ($\Delta T = 10$°C and 5°C, GDR is less than 15 %).

b) GDR results from measurement

The GDR for the obtained scattering information by 24 monopole antennas from the experimental measurement were calculated and presented in Figure 4.3, for different tube sizes in various temperature differences (temperature range of 25-45°C, with 5°C temperature steps). As in the simulation setup, the amplitude noise floor of the measurement system was $A_{dB}^{floor} = -80$ dB, and the results were plotted as a function of the system amplitude error A_{db}^{error} . The error levels for a network analyzer are $A_{dB}^{floor} < 1$ dB and phase error, $\theta^{error} < 1$ deg.

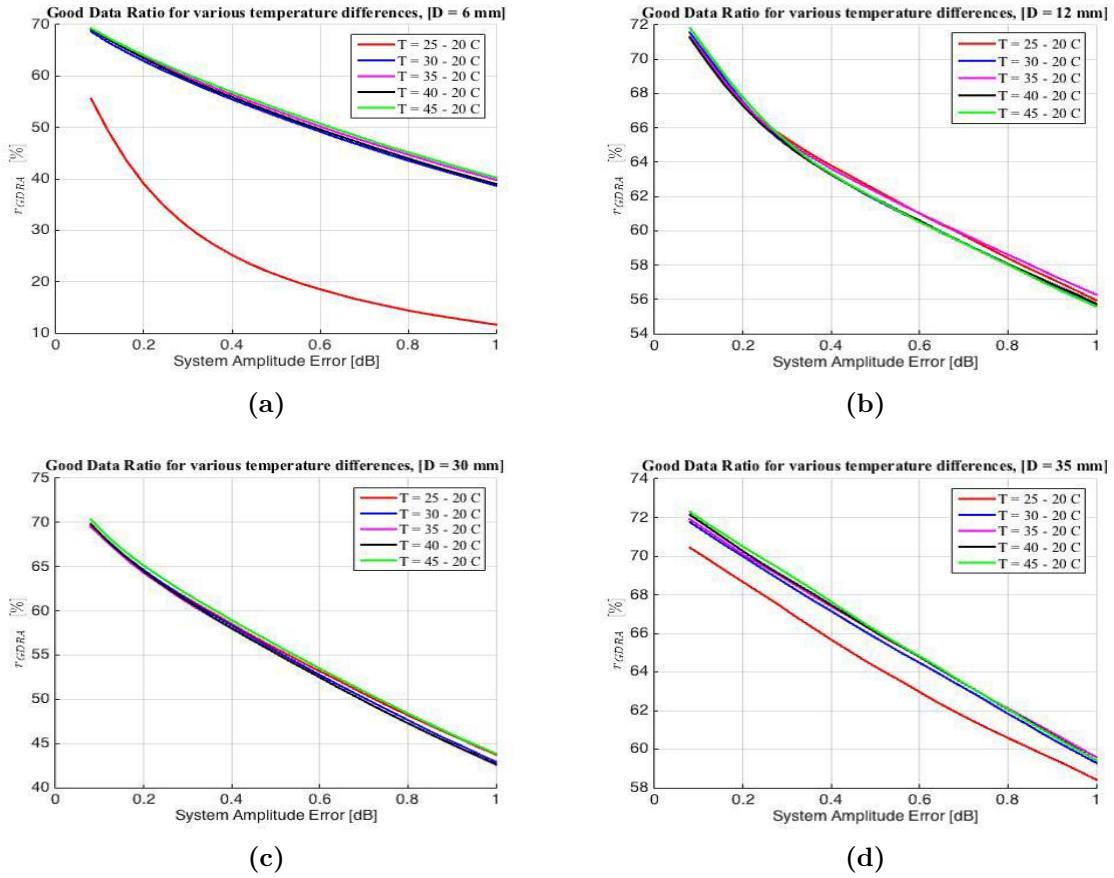

Figure 4.3: The GDR% as a function of the system amplitude error for the MT experimental setup; (a) heated tube with diameter 6 mm, located close to the wall of the phantom, (b) heated tube with diameter 12 mm, located close to the wall of the phantom, (c) heated tube with diameter 30 mm, located in the center of the phantom and (d) heated tube with diameter 35 mm, located close to the wall of the phantom.

From Figure 4.3 it can be noticed that the highest GDR, 72%, is obtained for the tube with diameter D = 35 mm, located close to the wall of the phantom, and the highest temperature difference (T = 45-20°C). The lowest GDR, 57%, is related to the tube with diameter D = 6 mm, located close to the wall, and the lowest temperature difference (T = 25-20°C). Results for different tube sizes with smaller temperature steps (1°C) as a function of amplitude, phase and also the amplitude-phase system error is plotted and described in Appendix D.

Figure 4.5 shows the calculated GDR for different tube sizes to determine the correlation between the GDR and the size of the heated region. Therefore, from the plot it can be noticed that for the selected temperature difference (T = 35-20°C), the 6mm tube has the smaller GDR (69%) and the 35mm tube shows the highest GDR (72%).

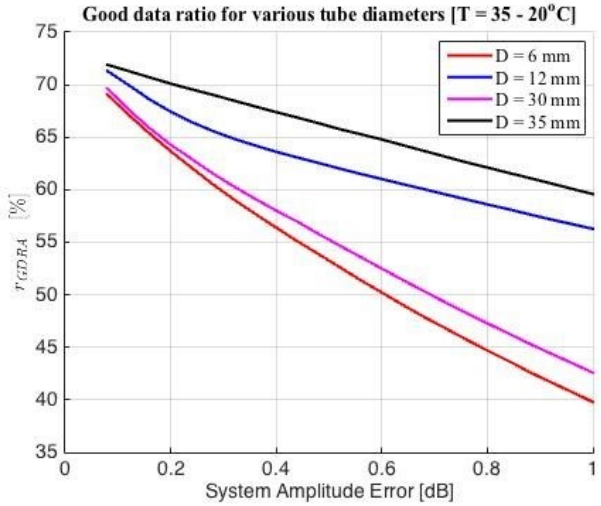

Figure 4.4: The amplitude based GDR%; various tube diameters and heated 35°C.

C) Image reconstruction

The obtained E-field from simulations for the reference temperature (T = 20°C) and also S-parameters for reference temperature and heated temperatures (T = 25, 30 35°C) were used in the developed algorithm for image reconstruction. The simulation was performed for nine frequency points; 400, 500, 600, 700, 800, 900, 1000, 1200 and 1400 MHz. The smoothness of the reconstructed images is **alfa**, which is defined in the algorithm. The introduced smoothness coefficient is highly sensitive to the frequency, image pixel size and field of view (FOV) in the reconstructed images. **alfa** can be varied between 0 to 1, in a way that the **alfa** = 0 results an image with maximum difference between its pixels. In contrast, **alfa** = 1 provides a very smooth image. The best performing **alfa** results in an image with high contrast only in the heated region and in other regions must show same value for entire non-heated region.

Figure 4.5 and 4.6 show the conductivity and permittivity reconstructed images for f = 500 MHz and 600 MHz respectively, and the temperature was increased 5°C.

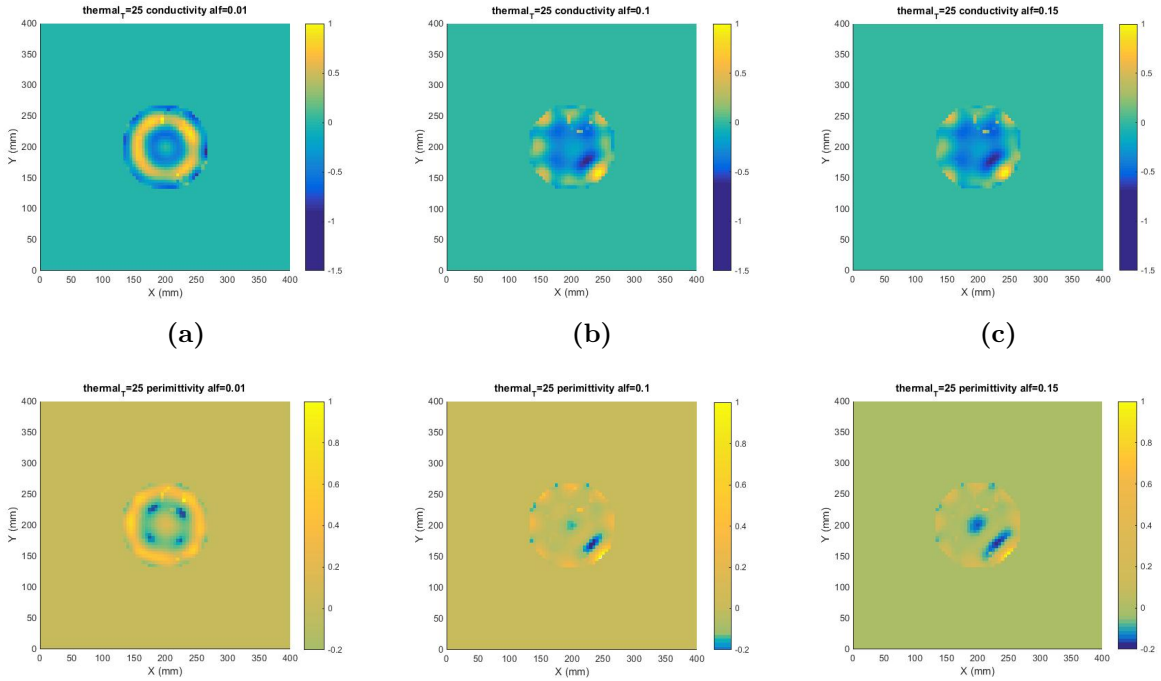

(a) **(b)** **(c)**

(d) **(e)** **(f)**

Figure 4.5: The complete phantom reconstructed images of relative permittivity and conductivity for f = 500 MHz and T = 25°C and **alfa** = 0.01, 0.1 and 0.15.

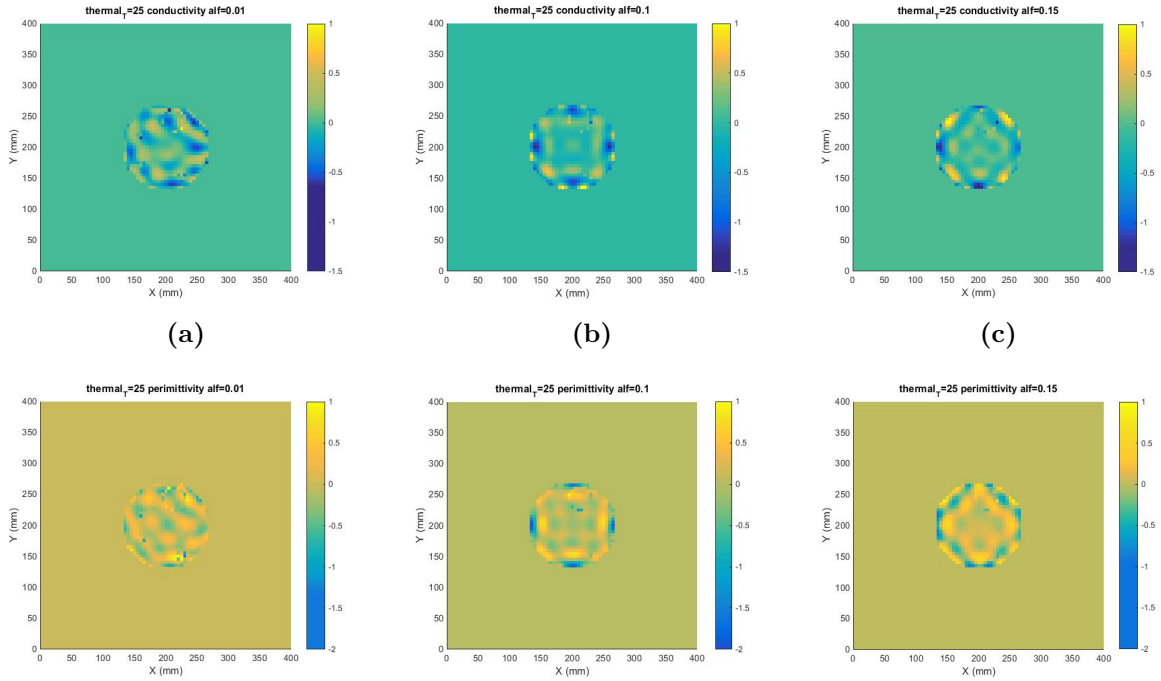

(a) **(b)** **(c)**

(d) **(e)** **(f)**

Figure 4.6: The complete phantom reconstructed images of relative permittivity and conductivity for f = 600 MHz and T = 25°C and alfa = 0.01, 0.1 and 0.15.

It can be observed that the smoothness of the reconstructed images are different for different **alfa**. In addition, the images for f = 500MHz in Figure 4.5 and f= 600MHz in Figure 4.6, are different in the same value for **alfa**.

Also, Figure 4.7 and 4.8 show the conductivity and permittivity reconstructed images for f = 500 MHz and 600 MHz respectively, and the temperature was increased 10°C.

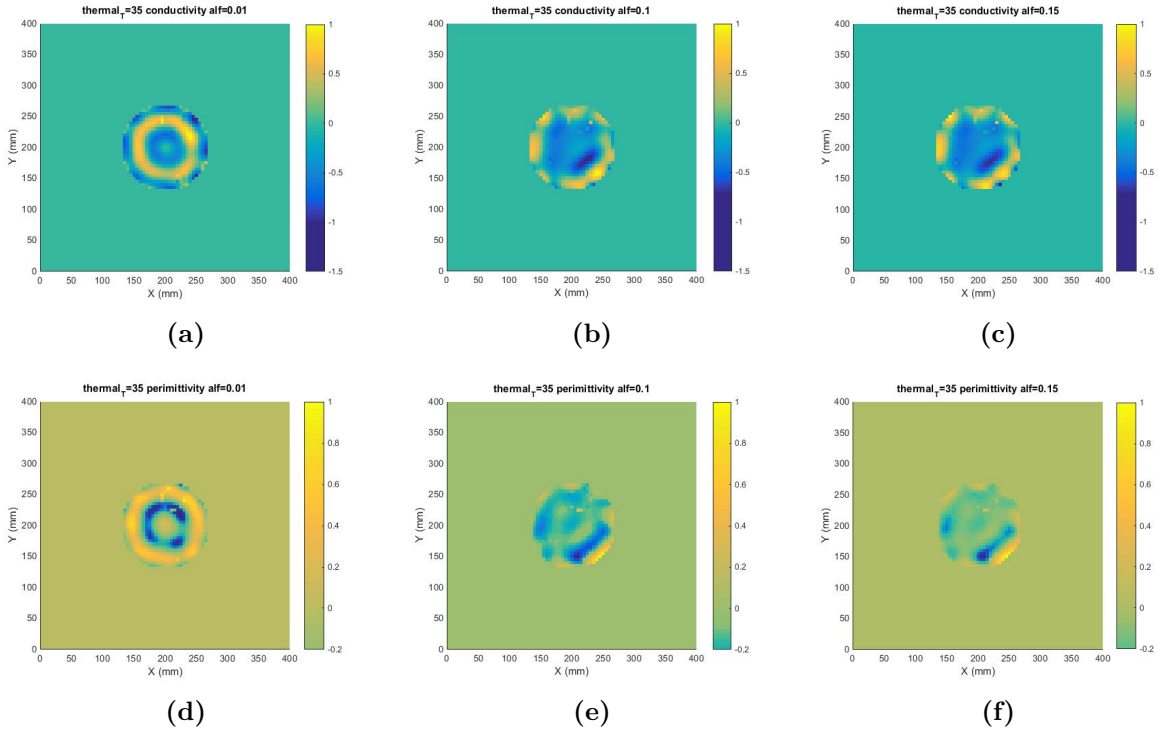

(a) **(b)** **(c)**

(d) **(e)** **(f)**

Figure 4.7: The complete phantom reconstructed images of relative permittivity and conductivity for f = 500 MHz and T = 35°C and alfa = 0.01, 0.1 and 0.15.

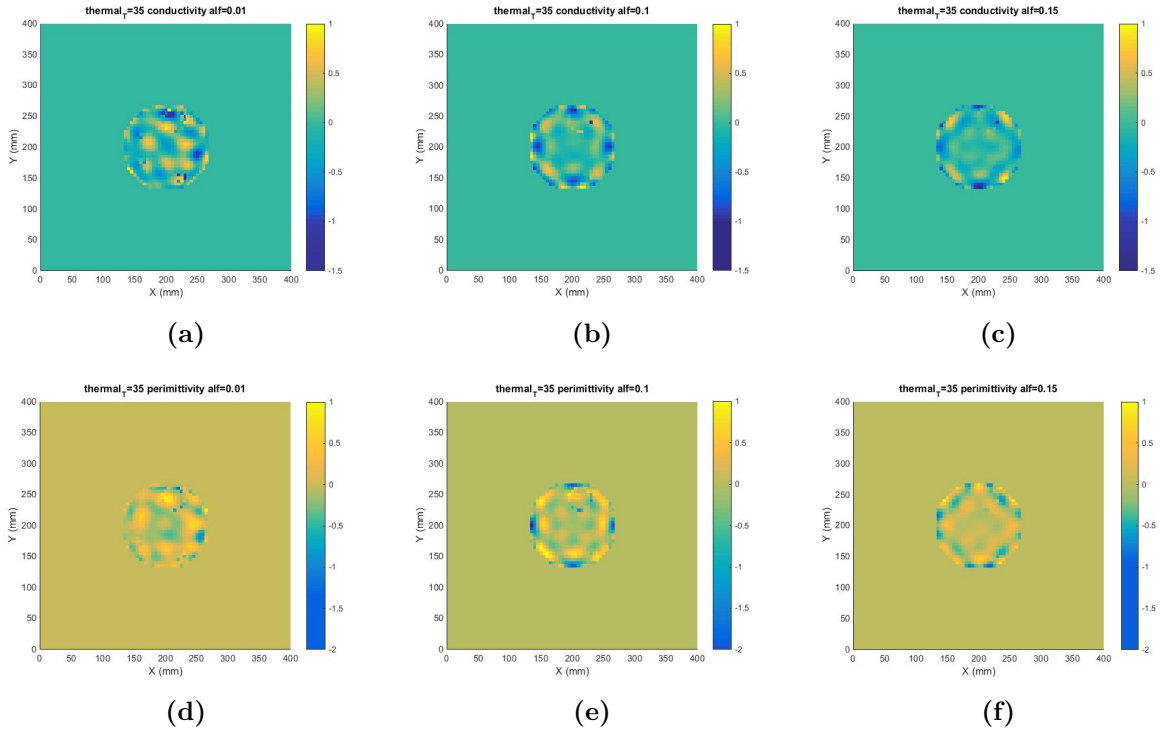

Figure 4.8: The complete phantom reconstructed images of relative permittivity and conductivity where f = 600 MHz, T = 35°C and alfa = 0.01, 0.1 and 0.15.

The same scenario can be seen for more temperature difference. The important outcome is that the temperature difference can not be recognizable in reconstructed images for whole phantom.

Therefore, to investigate the validation of the results, the heated region inside the tube $\phi = 35$ mm was reconstructed for different temperatures (T = 25, 30 35°C) as shown in Figure 4.9.

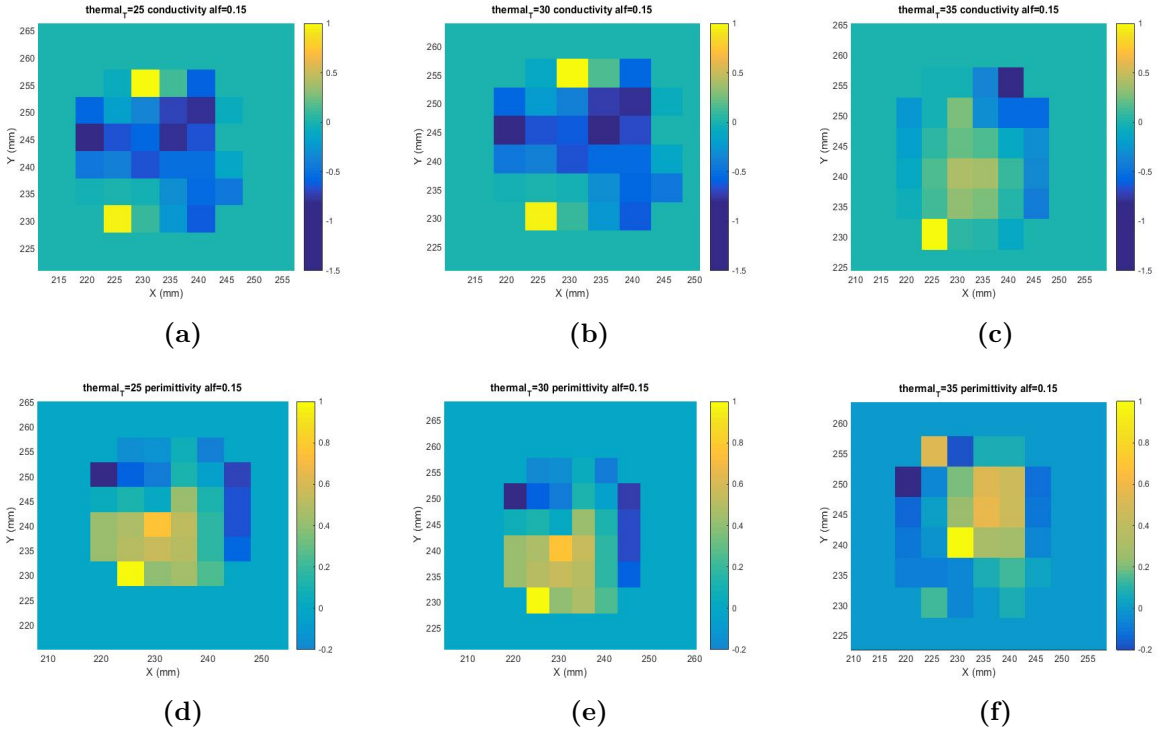

(a) **(b)** **(c)**

(d) **(e)** **(f)**

Figure 4.9: The heated region reconstructed images of relative permittivity and conductivity for f = 600 MHz, alfa = 0.15 and T = 25, 30 and 35°C.

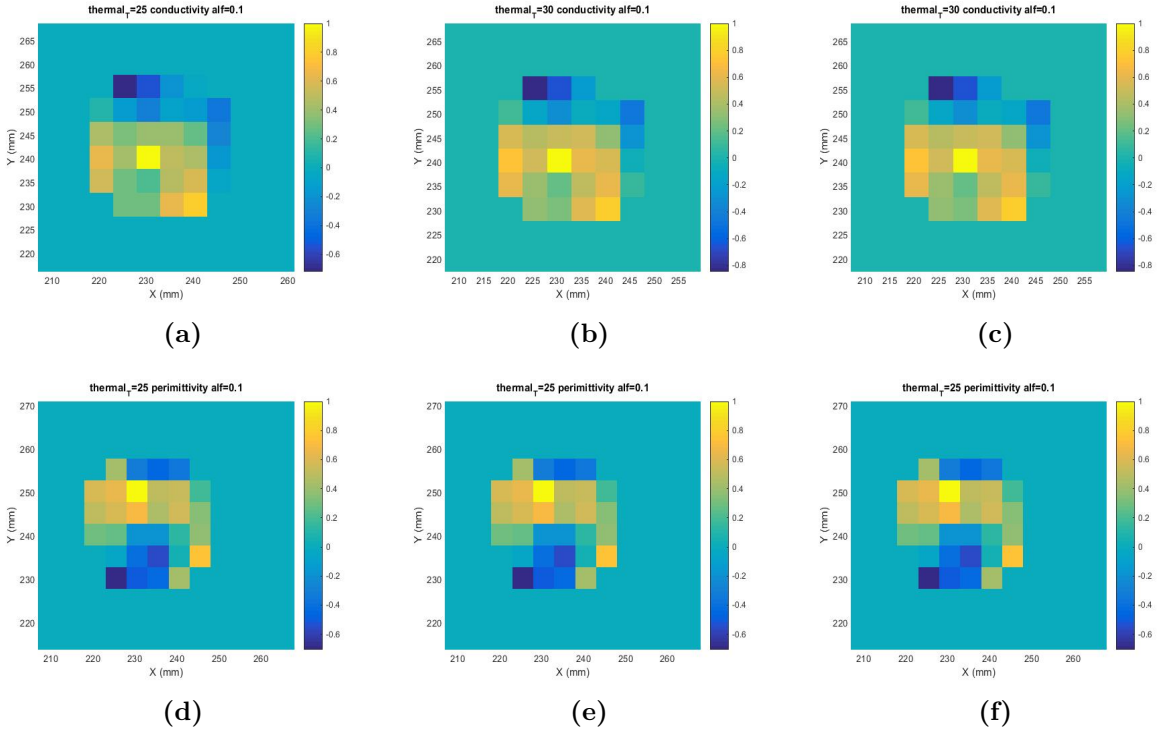

(a) **(b)** **(c)**

(d) **(e)** **(f)**

Figure 4.10: The heated region reconstructed images of relative permittivity and conductivity for f = 1000 MHz, alfa = 0.1 and T = 25, 30 and 35°C.

The Mean values for conductivity and permittivity of the heated region for temperatures increase of 5, 10 and 15°C for different frequencies 400, 500, 600 and 1000 MHz were calculated and plotted as in Figure 4.11.

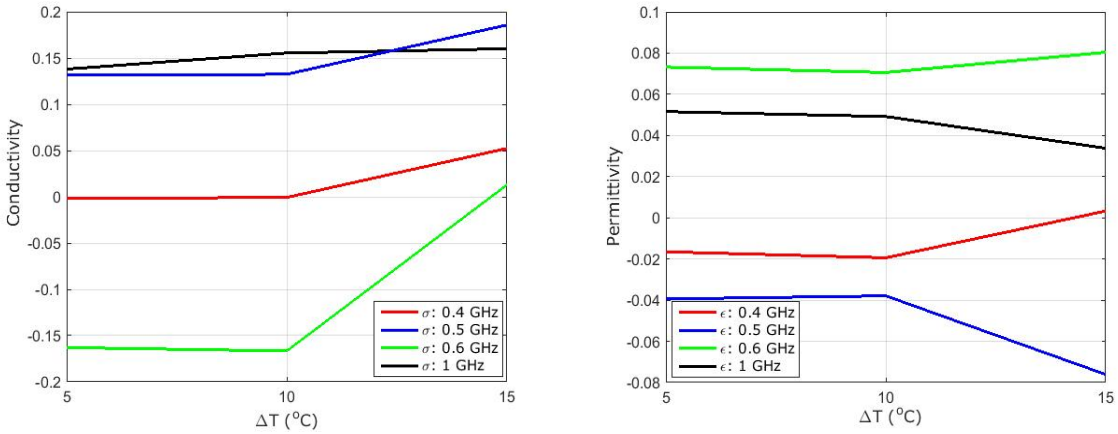

(a) **(b)**

Figure 4.11: Mean values of the reconstructed heated region as a function of temperature differences for different frequencies. (a) Relative conductivity (b) permittivity.

Figure 4.12 shows the experimental measurements of actual phantom temperature from previous study [57], which were used to evaluate the obtained simulation results in this work.

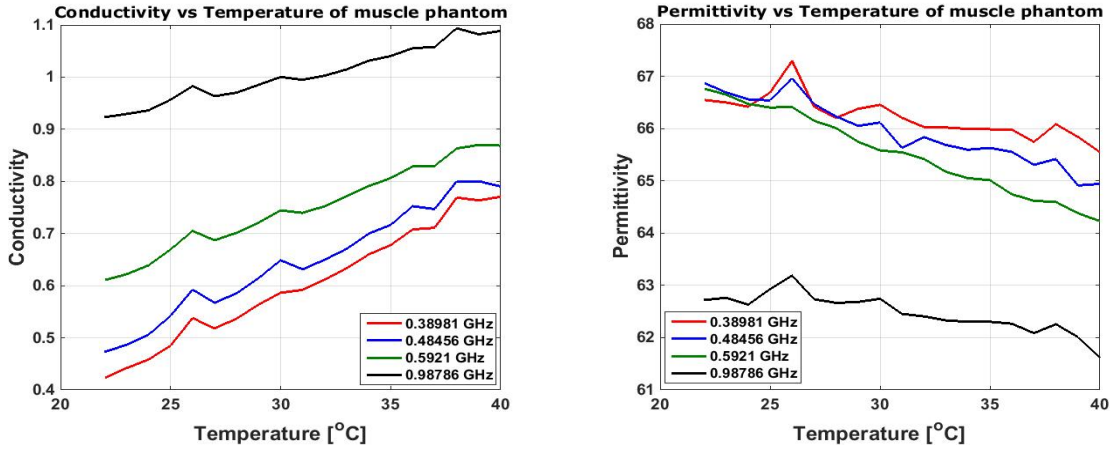

(a) **(b)**

Figure 4.12: The experimental measurements of the actual phantom temperature for different frequencies [57].(a) Relative conductivity (b) permittivity.

The result in Figure 4.11a for conductivity shows the same trend as in Figure 4.12a. However, the permittivity result in Figure 4.11b does not have same trend for all frequencies as in Figure 4.12b.

4.1.2 MWT with HT applicator

a) The effect of temperature on scattering data

Figure 4.13 shows the amplitude differences of scattering parameters for the new HT applicator, between the reference temperature (normal muscle phantom at 20°C) in the center of the simulated phantom in CST and the equivalent heated muscle phantom with 25°C. Figure 4.7a shows the highest difference around 0.37 GHz, which is not in the frequency range of the HT system. However, Figure 4.7b shows the differences for the HT system frequency range.

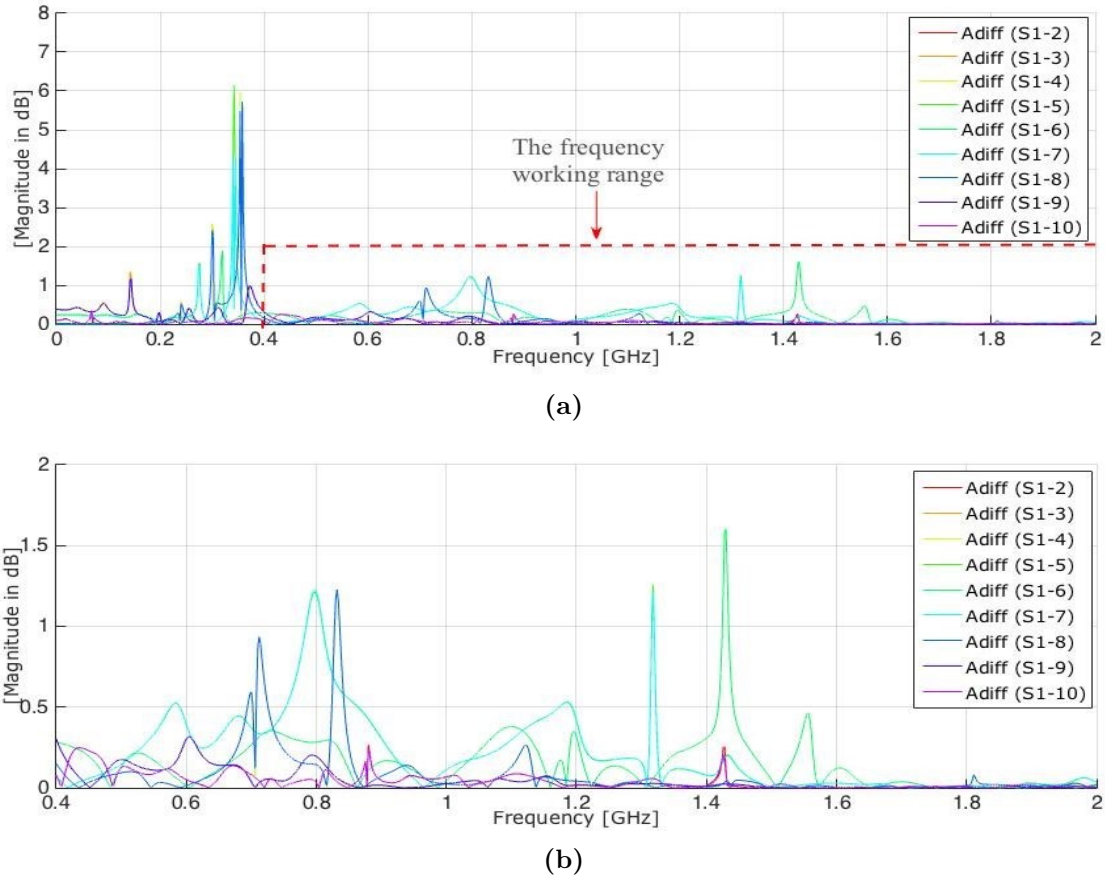

Figure 4.13: The amplitude difference of nine transmission coefficients for the new HT applicator; (a) the frequency range of 0-2 GHz, (b) the selected frequency working range of 0.4-2 GHz.

To achieve a better understanding of the computed results, the amplitude difference of S1-6, where antenna 1 is the transmitter and antenna 6 is the receiver, was chosen for all the simulated temperature differences (25, 30, 35, 40 and 45°C). In Figure 4.14 all the amplitude differences as a result of temperature changes, are plotted. It can be noticed that the highest difference is 1.8 dB which occurred at 1.43 GHz.

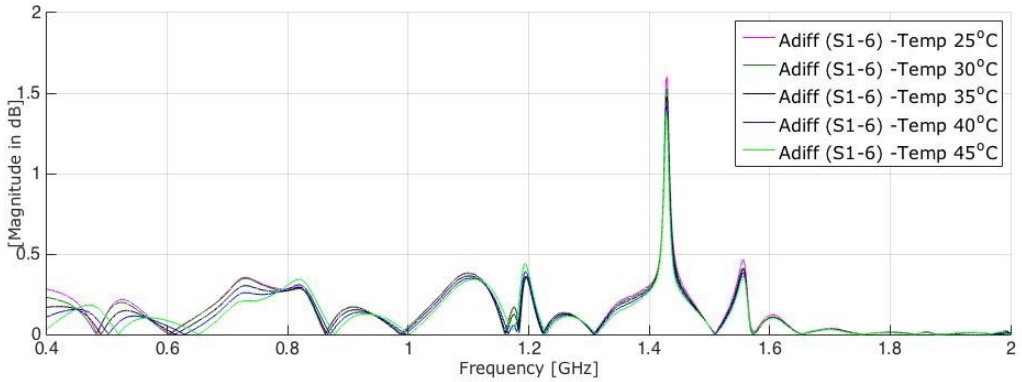

Figure 4.14: The amplitude difference of one transmission coefficient (S1-6).

b) HT applicator with two rings evaluation

The new HT applicator model with 10 bow-tie antennas placed in two rings, has improved the reflection coefficient in comparison with the previous HT applicator with one ring of 10 antennas, as shown in Figure 4.15.

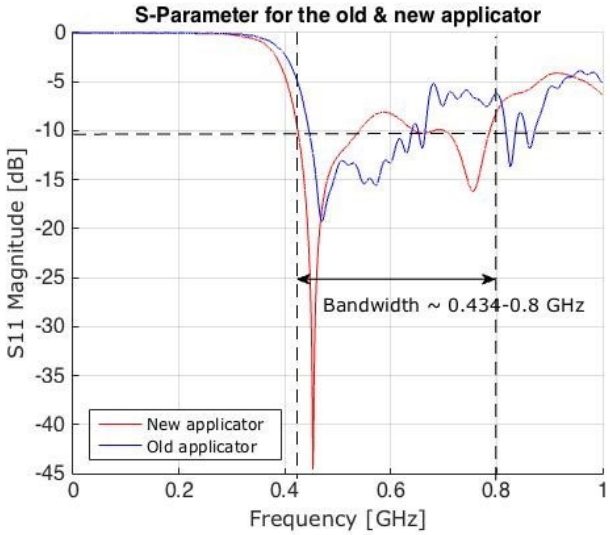

Figure 4.15: Comparison between reflection coefficients for the old and new applicator.

In order to evaluate the shape of the focus and the position of the hot spots, a qualitative analysis of SAR is done for the previous and the new antenna arrangement as shown in Figure 4.16.

Four different frequencies were considered (500 MHz, 600 MHz, 700 MHz and 800 MHz), where the target is in the center of the phantom. As it can be noticed for the old applicator (top) there is a better focus for lower frequencies (500 MHz and 600 MHz), in contrast, for the new applicator (bottom) it shows a better focus for higher frequencies (700 MHz and 800 MHz).

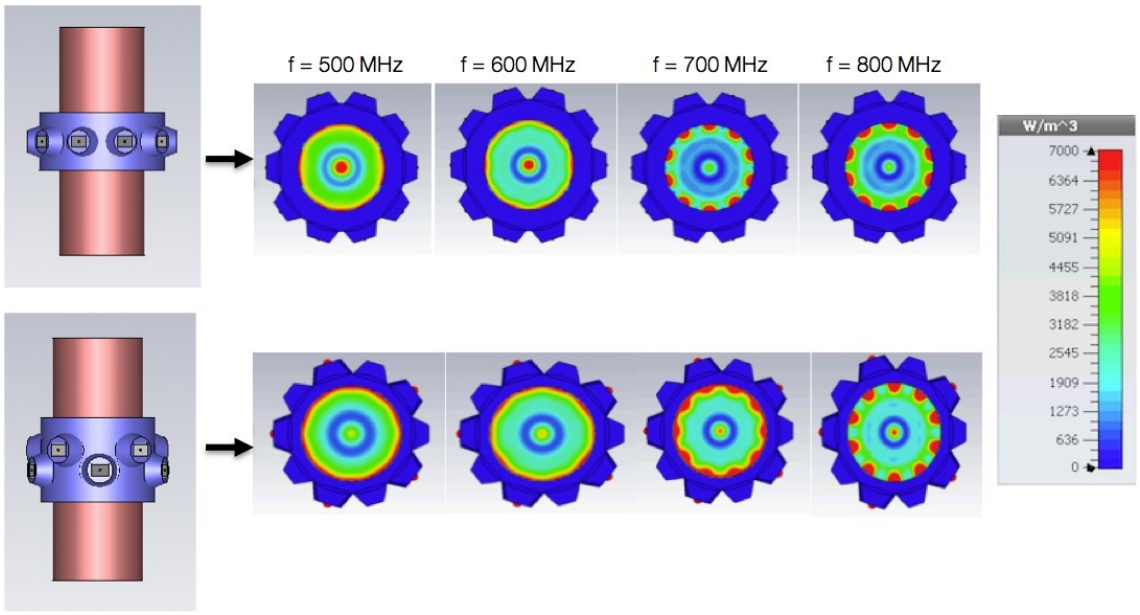

Figure 4.16: SAR distribution on an axial section for the previous applicator (top row) and the new applicator (bottom row).

GDR results from simulation

The GDR is presented for the new HT applicator in Figure 4.17 as a function of the system amplitude error for the tube with a diameter of 30 mm and located in the center of the phantom. Moreover, only one antenna was excited as a transmitter and the other 9 antennas were receiving the signal.

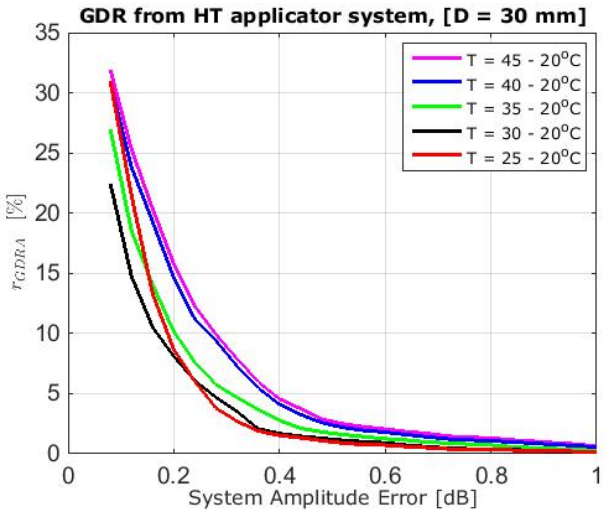

Figure 4.17: The amplitude-based GDR for the simulated HT applicator with different temperatures in the center of the phantom.

From the plot it can be noticed that the highest GDR is around 33% for T = 35°C and the lowest GDR is close to 20% for T = 30°C. It also can be noted that the

largest number of data point in all the simulated temperatures are detectable with an amplitude error less than 0.3 dB.

4.2 MR-thermometry results

4.2.1 Measurements results

The experiments were performed with the described phantom setup (Section 3.4). The temperature-time curves were directly measured with 2 Bowman thermistors (one inside the phantom and another inside the tube outside the phantom as shown in Figure 3.19), and compared with the real temperature (set in the water pump). All the MR datasets were processed with the SHPV and the obtained results are shown in Figure 4.18 and 4.19.

1) Body coil

Figure 4.10a and 4.10b show the phase images for the reference and heated water temperature respectively. In Figure 4.10c the phase difference for ΔT= 15°C is shown. Also a circle mask, in the center of the image and with the radius of r = 75 mm was used as in Figure 4.10d shown all the background phase artifacts are removed. The highest phase difference can be seen in the center of the phantom. However, there are some phase differences in other parts of the image that is not as big as inside the centered tube.

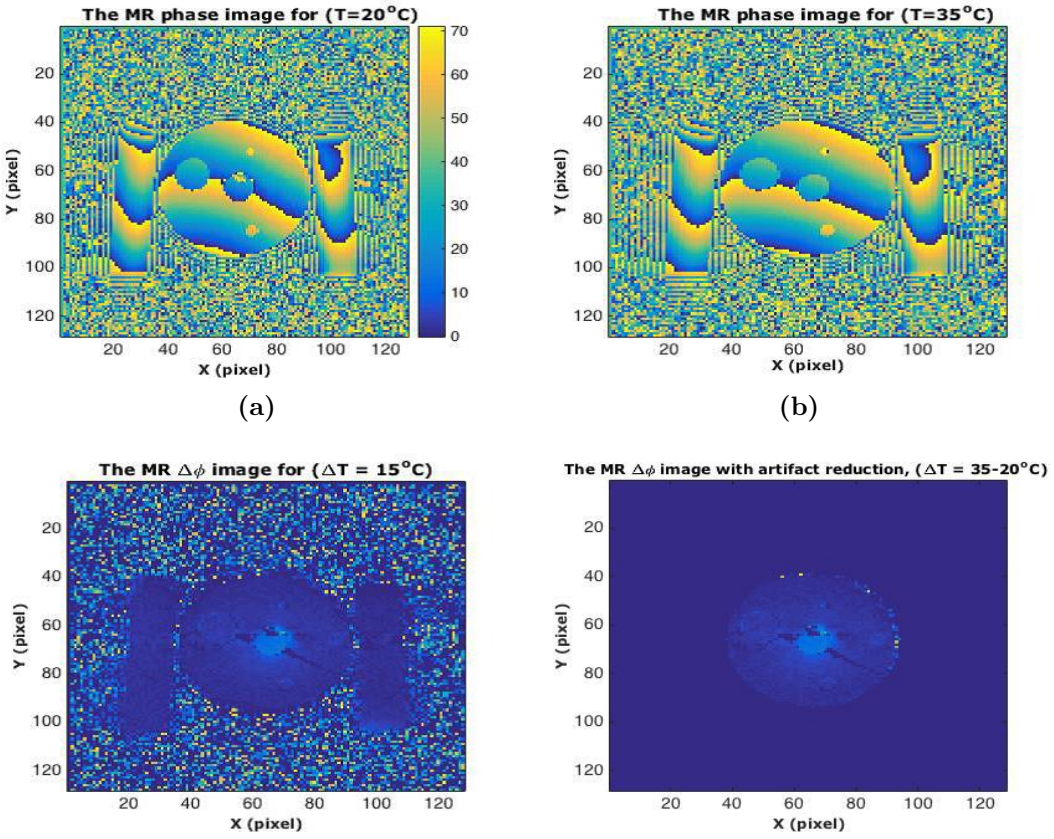

Figure 4.18: The phase images for the body coil for (a) the reference temperature (T = 20°C), (b) the elevated temperature (T = 35°C) for the 30 mm (in diameter) tube at the center of the phantom, (c) the phase difference from (a) and (b), and (d) the phase difference with some artifact reduction in the background.

Head coil

The same process was performed for the datasets that were obtained for MR tomography with the head coil where four oil bags were used instead of oil bottles. From Figure 4.11c and 4.11d it can clearly be observed that there is a high phase difference in the center of the phantom.

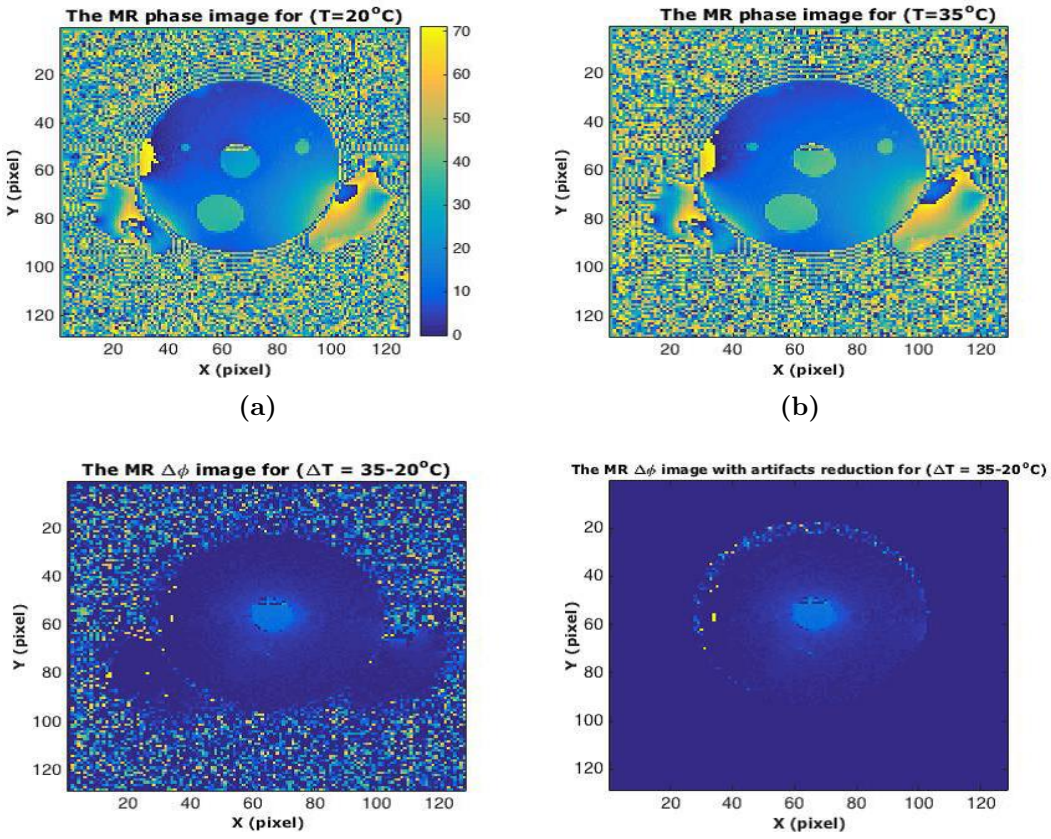

Figure 4.19: The phase images for head coil for (a) the reference temperature (T = 20°C), (b) the elevated temperature (T = 35°C) for the 30 mm (in diameter) tube at the center of the phantom, (c) the phase difference from (a) and (b), and (d) the phase difference with some artifacts reduction in the background.

Figure 4.20 shows the phase differences for various temperature differences. In addition, these phase differences were used to calculate the α-parameter. From the results in Figure 4.19 the highest $\Delta\phi = 14$ rad is in the central tube where the circulating water was heated up to 35°C ($\Delta T = 15$°C), and the lowest $\Delta\phi = 2$ rad was acquired for the water temperature 25°C ($\Delta T = 3$°C).

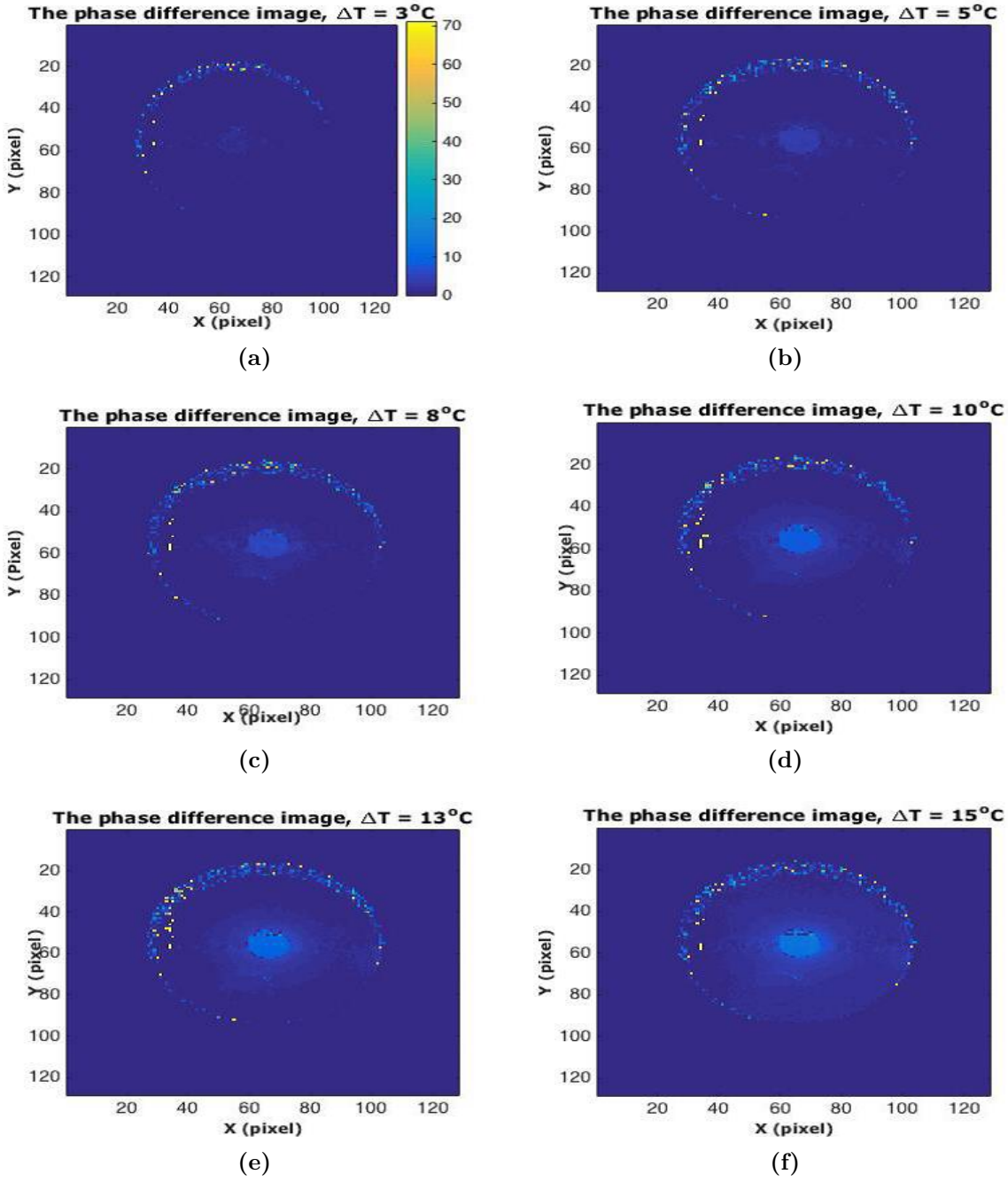

Figure 4.20: The phase difference images, with various temperature differences for the tube D = 30 mm.

4.2.2 PRFS accuracy and α-calibration

Eq. 3.23 was used to calculate the PRF change per degree Celsius (α-parameter), which has a significant effect on the accuracy of the ΔT calculation. A Linear regression line was used which provides the best-fit line with the lowest prediction error. Figure 4.21 shows the obtained linear regression line (the red dashed line) for all $\Delta\phi$ as a function of the ground-truth temperature. It also can be noted that the

obtained best-fit line starts from origin. It means the $\Delta T = 0$ gives $\Delta\phi = 0$.

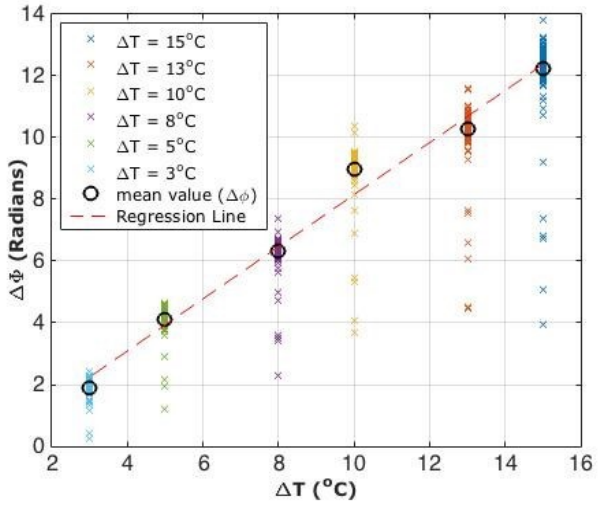

(a)

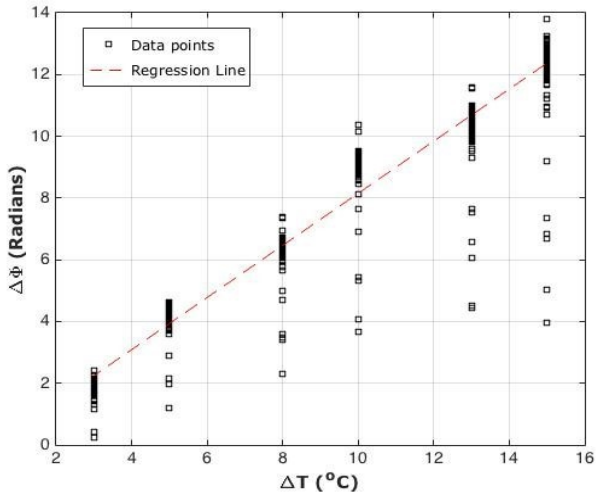

(b)

Figure 4.21: PRFS phase as a function of the ground-truth temperature, (a) by use of the mean value at each temperature increase and (b) by use of the best fit within all the data points.

In Figure 4.21a, the mean value of $\Delta\phi$ for each ΔT was calculated, then the linear regression line was obtained from the mean values and in Figure 4.21b, all $\Delta\phi$ values for all ΔT were calculated as a long vector and the best fit line was calculated within all the data points. Finally, from the slope of the obtained line, the calibrated α was calculated to be 0.000692 ppm/°C.

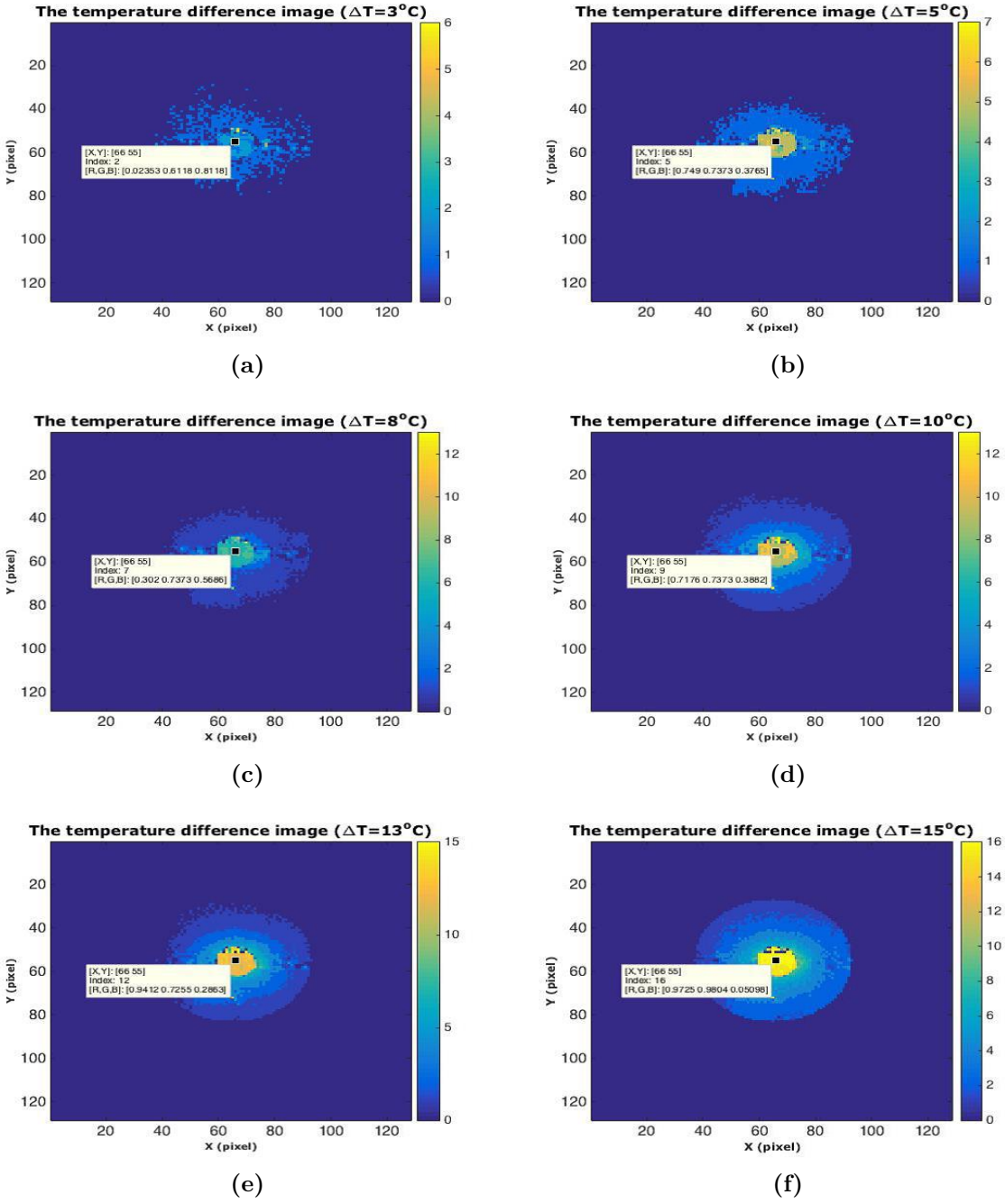

Figure 4.22: The relative temperature images for the tube D = 30 mm.

The calibrated α was replaced in Eq 3.23 and the relative temperature differences were calculated. Figure 4.22 shows the calculated temperature for each reference temperature. To have a better observation of the obtained results, the temperature of the central pixel in each image is labeled. The reference ΔT for each image is the temperature that was used in the pump and the marker in the center of each image is the calculated ΔT from Eq. 3.23. The maximum error between these two values results in the accuracy of the measurement, which is ± 1°C.

5

Discussion

5.1 MW-thermomtry

5.1.1 MWT with tomography (monopole) system

Figure 5.1 shows a comparison between simulation and measurement results of scattering data. The results verify the experimental data in comparison with the simulation that was performed for the same condition.
The purpose of the simulation was to determine the accuracy of the measurements with the experimental setup. Figure 5.1 shows the simulated and measured transmission coefficient (S_{12}) and reflection coefficient (S_{11}) between antennas number 01 and 02.

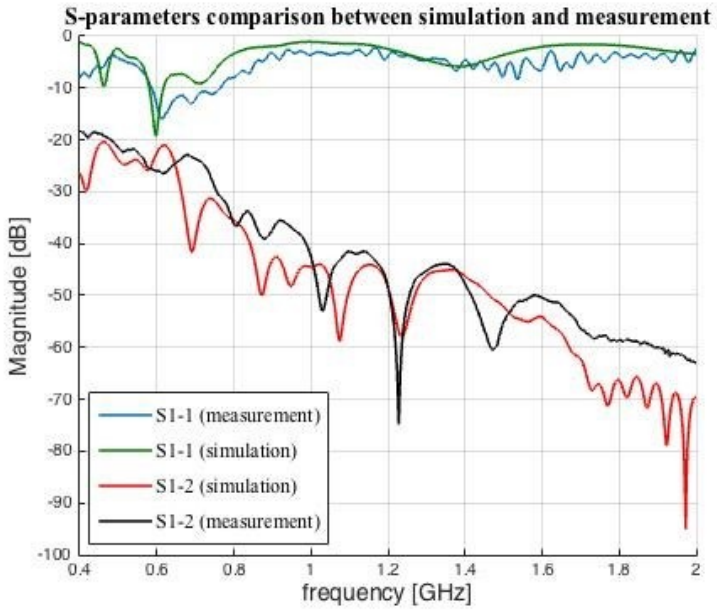

Figure 5.1: Comparison between S-parameters for simulation and measurement.

From the plot, it can be concluded that there is an excellent agreement between measurement and simulation.

a) GDR evaluation

The GDR for the experimental measurement indicates that for the larger tubes, and tubes located close to the phantom wall, a greater number of useful data points is generated. Due to the detection of less information for a small tube deep inside the phantom is more challenging. Also a higher temperature difference provides a larger number of data points that are detectable than a smaller temperature difference. The same trend is observed when a smaller temperature step of 1°C was chosen, where in the tube $\phi = 6$ mm the number of detectable data for the first 5 temperatures (21, 21, 22, 23, 24 and 25°C) is significantly lower than the last 5 temperatures (26, 27, 28, 29 and 30°C).
It can be concluded that the larger the heated region, the greater the GDR(%), and the GDR(%) increases if the heated region is closer to the surface of the phantom. Certainly, the diameters above the 30 mm results in better detectable data. While for the smaller diameters such as 12 mm results in lower amount of detectable data, specially for placed deep location in the phantom. There is also a strong correlation between the temperature differences in the heated region and the GDR and it can be noted that the GDR reduces as the system amplitude error increases.
The comparison between obtained simulation results for MW and HT systems, gives the same quality of GDR for both system, which is around 33%. However, the obtained GDR% for simulation measurements is 50% less than the experimental measurements. Possible reason for this difference might be for underestimation of the real phantom dielectric properties in simulations.

b) Image reconstruction

The reconstructed images of the phantom obtained from simulations data were investigated for different frequencies and different smoothness coefficient values. The results images did not show a high temperature resolution for different temperatures increase. Therefore, the heated region inside the tube ($\phi = 35$ mm) were quantitatively analyzed by determining the mean values of the permittivity and conductivity over the reconstructed heated region. The obtained results were compared with the experimental measurements from previous study [57], where the absolute values for permittivity and conductivity were measured. The study showed the mean values for conductivity follow the trend, i.e. the conductivity increase with increased temperature. The results for permittivity are more difficult to evaluate as the experiment increase or decrease vary for different frequencies.

5.1.2 MWT with HT applicator

a) HT applicator with two rings

For the developed HT applicator, the working frequency does not change significantly in Figure 4.6. There is also a strong correlation between the reflection coefficient and thickness of the surface water-bolus, which for the new applicator is 20 mm thick (half of the thickness in the old applicator with 40 mm). Therefore, there is less reflection and more transmission in the working bandwidth of the antennas. The results for SAR distribution show the delivered energy in the new applicator

with 10 bow-tie antennas located in two rings and is concentrated in the central region, especially at high frequencies, which in comparison with the old applicator with the same number of antennas placed in one ring is a significant improvement.

b) The effect of temperature changes on scattering data

The aim of performing simulations was to investigate the temperature change in the heated region of the simulated phantom and how this affects the scattering data within the working frequency. The simulations showed small differences between different temperatures. However, it must be considered that in all the simulations only one antenna was excited, which can be an important reason for not seeing significant change in the scattering data. In addition, the simulated tube in the heated region with the wall thickness of 3 mm can effect the concentration of delivered energy.

c) GDR evaluation

The measured GDR(%) for the simulated HT applicator in comparison with the simulated MW tomography system showed very similar values for the highest and lowest obtained GDR, 30% and 20% respectively. However, the obtained simulated results are much lower than the measurement results.

5.2 MR-thermometry

5.2.1 Measurements evaluation

For MR tomography with the body coil in comparison with the head coil, the phase images have a higher phase drift. The reason for this can be explained by the size of the body coil that was much bigger than the size of the phantom in comparison with the head coil. In a real clinical treatment, the head coil can not be used to small space for fit applicator.
Although the results validate the chosen experimental setup, there are some areas in which to improve the current setup.

5.2.2 PRFS accuracy and α calibration

From the results it can be noted that if the α-parameter is correct, the PRFS phase change $\Delta\phi$ for all the measured phases plotted as a function of reference temperature (the temperature of the pump) should agree with the linear regression line. Moreover, the slope of the linear regression provides the value of the α-parameter.

6
Conclusion

6.1 Summary

In this work a phantom was developed to simulate the heating action by use of water circulation inside the tubes that was suitable for both MR and MW thermometry. Simulation and experimental measurements were performed to investigate the feasibility of MW-thermometry for hyperthermia treatment with both MW tomography and HT applicator systems. The results showed that the GDR for highest amplitude error 1 dB is 40 for 6 mm tube and 60 for 35 mm for $\Delta T = 5°\text{C}$. Simulated values for both MW systems were agreed to each other, while gave smaller number of good data than experimental measurement. Possible reason might be underestimation of real phantom dielectric properties in simulations.
The 3D fast reconstruction for full phantom images did not provide clear images of temperature change especially for deep seated locations. The heated region therefore reconstructed and studied which it provided a comparison between dielectric properties trends for simulated and experimental measurements.

The MR-thermometry was used as a reference method to evaluate the thermal resolution and accuracy. For this, two setups for the MR scanner were applied; 1) MR body coil and 2) MR head coil. The results with head coil set showed a lower phase drift than body coil set. However, in clinical treatment the head coil can not be used due to small space for HT applicator, even if it causes more phase drift.
The temperature images for MR measurement then was obtained by calculating the α parameter, as the PRFS thermal coefficient (the PRF change per degree Celsius). The calculated α value for this work was 0.000692 $ppm/^o\text{C}$. With this value of α, the temperature accuracy of the measurement was $\pm 1°\text{C}$, which it is same for the MR temperature images with the clinical software (SHPV).

6.2 Suggestions for future work

The following work can be done to improve the current system:

- The algorithm for 3D fast reconstruction needs to improve due to the poor reconstructed images. The possible solutions are number of antennas, in which more antennas may need to increase the temperature accuracy. The other solution is to use multiple frequency instead single frequency. Image reconstruction can be performed with different frequencies to find the best performing

smoothness coefficient and see how the reconstructed images are affected by this.

- Experimental measurement with HT applicator will have to be performed to evaluated the feasibility and also accuracy of the MWT with the results from MRT and MW tomography system.
- The temperature resolution for MRT needs to be improved to maximize the accuracy of the measurement. The MRT measurement can be repeated for 6 mm tube. Also, the algorithm for can improve to calculate the rel temperature in phantom and in heated region inside the tube.

Bibliography

[1] D. Parkin, F. Bray, and J. Ferlay, "Global cancer statistics, 2002," 2005.

[2] D. M. Cognetti, R. S. Weber, and S. Y. Lai, "Head and neck cancer," Cancer, vol. 113, no. S7, pp. 1911-1932, 2008.

[3] H. D. Trefná, "Advanced in microwave hyperthermiaa treatment using time reversa," PhD thesis, 2010.

[4] G. van Rhoon and P. Wust, "Introduction: Non-invasive thermometry for thermotherapy," International Journal of Hyperthermia, vol. 21, no. 6, pp. 489-495, 2005.

[5] C. J. Bolomey, L. Jofre, and G. Peronnet, "On the possible use of microwaveactive imaging for remote thermal sensing," Microwave Theory and Techniques, IEEE Transactions on, vol. 31, no. 9, pp. 777-781, 1983.

[6] W. C. M. Numan, L. W. Hofstetter, G. Kotek, J. F. Bakker, E. W. Fiveland, G. C. Houston, G. Kudielka, D. T. B. Yeo, and M. M. Paulides, "Exploration of MR-guided head and neck hyperthermia by phantom testing of a modified prototype applicator for use with proton resonance frequency shif thermometry., "International journal of hyperthermia : the official journal of European Society for Hyperthermic Oncology, North American Hyperthermia Group, vol. 30, no. 3, 2014.

[7] V. Rieke and K. B. Pauly, "MR thermometry," Journal of Magnetic Resonance Imaging, vol. 27, no. 2, pp. 376-390, 2008.

[8] M. M. Paulides, J. F. Bakker, M. Linthorst, J. van der Zee, Z. Rijnen, E. Neufeld, P. M. T. Pattynama, P. P. Jansen, P. C. Levendag, and G. C. van Rhoon, "The clinical feasibility of deep hyperthermia treatment in the head and neck: new challenges for positioning and temperature measurement.," Physics in medicine and biology, vol. 55, no. 9, pp. 2465-2480, 2010.

[9] P. Vaupel and F. Kallinowski, "Physiological effects of hyperthermia," in Hyperthermia and the Therapy of Malignant Tumors (C. Streffer, ed.), vol. 104 of Recent Results in Cancer Research, pp. 71-109, Springer Berlin Heidelberg, 1987.

[10] P. Meaney, K. Paulsen, M. Fanning, D. Li, and Q. Fang, "Image accuracy improvements in microwave tomographic thermometry: phantom experience," International journal of hyperthermia, vol. 19, no. 5, pp. 534-550, 2003.

[11] R. Hoffman, M. Monga, and S. Elliott, "Microwave thermotherapy for benign prostatic hyperplasia," 2007.

[12] K. Leopold and P. D. Issels, "Thermoradiotherapy and thermochemotherapy for sarcomas," pp. 147-158, 1996.

[13] M. Peller, V. Kurze, R. Loeffler, and S. Pahernik, "Hyperthermia induces t1 relaxation and blood flow changes in tumors. a MRI thermometry study in vivo," 2003.

[14] K. Sugimachi, K. Kitamura, K. Baba, M. Ikebe, M. Morita, H. Matsuda, and H. Kuwano, "Hyperthermia combined with chemotherapy and irradiation for patients with carcinoma of the oesophagus–a prospective randomized trial read more: http://informahealthcare.com/doi/abs/10.3109/02656739209021783,"1992.

[15] H. V. R and D. F, "Thermoradiotherapy and thermochemotherapy for pediatric tumors," 1996.

[16] O. MA and A. Boehle, "Treatment options for BCG failures," 2006.

[17] R. Issels, A. S, and C. Wendtner, "Neoadjuvant chemotherapy combined with regional hyperthermia (RHT) for locally advanced primary or recurrent high risk adult soft-tissue sarcomas (STS) of . . . ," 2001.

[18] J. Lagendijk, "Hyperthermia treatment planning," Physics in medicine and biology, vol. 45, no. 5, 2000.

[19] M. M. Paulides, P. R. Stauffer, E. Neufeld, P. F. Maccarini, A. Kyriakou, R. A. Canters, C. J. Diederich, J. F. Bakker, and G. C. Van Rhoon, "Simulation techniques in hyperthermia treatment planning," International Journal of Hyperthermia, vol. 29, no. 4, pp. 346-357, 2013.

[20] M. de Bruijne, D. Wielheesen, J. van der Zee, N. Chavannes, and G. Van Rhoon, "Benefits of superficial hyperthermia treatment planning: Five case studies, " International Journal of Hyperthermia, vol. 23, no. 5, pp. 417-429, 2007.

[21] M. Weiser and A. Schiela, "Function space interior point methods for pde constrained optimization," PAMM, vol. 4, no. 1, pp. 43-46, 2004.

[22] O. Schenk, M. Manguoglu, A. Sameh, M. Christen, and M. Sathe, "Parallel scalable pde-constrained optimization: antenna identification in hyperthermia cancer treatment planning," Computer Science-Research and Development, vol. 23, no. 3-4, pp. 177-183, 2009.

[23] M. A. Flower, Webb's physics of medical imaging. CRC Press, 2012.

[24] N. J. McDannold and F. A. Jolesz, "Magnetic resonance image-guided thermal ablations," Topics in Magnetic Resonance Imaging, vol. 11, no. 3, pp. 191-202, 2000.

[25] D. Le Bihan, J. Delannoy, and R. L. Levin, "Temperature mapping with mr imaging of molecular diffusion: application to hyperthermia.," Radiology, vol. 171, no. 3, pp. 853-857, 1989.

[26] M. R. Tarasek, R. Pellicer, L. W. Hofstetter, W. C. M. Numan, J. F. Bakker, G. Kotek, P. Togni, R. F. Verhaart, E. W. Fiveland, G. C. Houston, G. C. van Rhoon, M. M. Paulides, and D. T. B. Yeo, "Validation of MR thermometry: Method for temperature probe sensor registration accuracy in head and neck-phantoms, " International Journal of Hyperthermia, vol. 30, no. 2, p. 142149, 2014.

[27] S. K. Smith, "Theoretical feasibility study of preferential hyperthermia using silicon carbide inserts," Master thesis, 2004.

[28] J. Bamber and C. Hill, "Ultrasonic attenuation and propagation speed in mammalian tissues as a function of temperature," 1979.

[29] W. Straube and R. M. Arthur, " Theoretical estimation of the temperature dependence of backscattered ultrasonic power for noninvasive thermometry," Ultrasound in medicine and biology, vol.20, no.9, pp.915-922, 1994.

[30] R. Nasoni, T. Bowen, W. Connor, and R. Sholes, "In vivo temperature dependence of ultrasound speed in tissue and its application to noninvasive temperature monitoring," Ultrasonic Imaging, vol. 1, no. 1, pp. 34-43, 1979.

[31] S. Ueno, M. Hashimoto, and H. Fukukita, "Ultrasound thermometry in hyperthermia," 1990.

[32] T. P. Ryan and T. Z. Wong, "Thermal treatment of tissue with image guidance," in Thermal Treatment of Tissue with Image Guidance, vol. 3594, 1999.

[33] B. Fallone, P. Moran, and E. Podgorsak, " Noninvasive thermometry with a clinical xray CT scanner," 1982.

[34] M. Miyakawa, " Tomographic measurement of temperature change in phantoms of the human body by chirp radar type microwave computed tomography," Medical and biological engineering and computing, vol.31, no.1, pp.S31-S36, 1993.

[35] J. Chang, K. Paulsen, P. Meaney, and M. Fanning, "Non-invasive thermal assessment of tissue phantoms using an active near field microwave imaging technique," International journal of hyperthermia, vol. 14, no. 6, pp. 513-534, 1998.

[36] P. Meaney, M. Fanning, K. Paulsen, D. Li, S. Pendergrass, Q. Fang, and K. Moodie, "Microwave thermal imaging: initial in vivo experience with a single heating zone," International journal of hyperthermia, vol. 19, no. 6, pp. 617-641, 2003.

[37] H. D. Trefná, A. Fhager, J. Hellman, and M. Persson, "Microwave thermal imaging:towards hyperthermia applications," 2010.

[38] J. Gellermann, W. Wlodarczyk, B. Hildebrandt, H. Ganter, A. Nicolau, B. Rau, W. Tilly, H. Fahling, J. Nadobny, and R. Felix, "Noninvasive magnetic resonance thermography of recurrent rectal carcinoma in a 1.5 tesla hybrid system," Cancer Research, vol. 65, no. 13, pp. 5872-5880, 2005.

[39] T. Nelson and S. Tung, "Temperature dependence of proton relaxation times in vitro," 1987.

[40] M. Peller, H. Reinl, and A. Weigel, "T1 relaxation time at 0.2 tesla for monitoring regional hyperthermia: feasibility study in muscle and adipose tissue," 2002.

[41] K. Cheng and M. Hernandez, "Magnetic resonance diffusion imaging detects structural damage in biological tissues upon hyperthermia," 1992.

[42] J. Gellermann, W. Wlodarczyk, A. Feussner, H. Fähling, J. Nadobny, B. Hildebrandt, R. Felix, and P. Wust, "Methods and potentials of magnetic resonance imaging for monitoring radiofrequency hyperthermia in a hybrid system," International journal of hyperthermia, vol. 21, no. 6, pp. 497-513, 2005.

[43] J. Hindman, " Proton resonance shift of water in the gas and liquid states," The Journal of Chemical Physics, vol. 44, no. 12, pp. 4582-4592, 1966.

[44] W. G. Schneider, H. Bernstein, and J. Pople, "Proton magnetic resonance chemical shift of free (gaseous) and associated (liquid) hydride molecules," The Journal of Chemical Physics, vol. 28, no. 4, pp. 601-607, 1958.

[45] C. R. Wyatt, "Development of mr thermometry strategies for hyperthermia of extremity and breast tumors," PhD thesis, 2010.

[46] D. W. McRobbie, E. A. Moore, M. J. Graves, and M. R. Prince, MRI from Picture to Proton. 2010.

[47] S. Dehkharghani, H. Mao, L. Howell, X. Zhang, K. Pate, P. Magrath, F. Tong, L. Wei, D. Qiu, C. Fleischer, and J. Oshinski, "Proton resonance frequency-chemical shift thermometry: Experimental design and validation toward High Resolution noninvasive temperature monitoring and in vivo experience in anon-human primate model of acute ischemic stroke," American Journal of Neuroradiology, vol. 36, no. 6, pp. 1128-1135, 2015.

[48] K. Hynynen, O. Pomeroy, D. N. Smith, P. E. Huber, N. J. McDannold, J. Kettenbach, J. Baum, S. Singer, and F. A. Jolesz, "Mr imaging-guided focused ultrasound surgery of fibroadenomas in the breast: A feasibility study 1," Radiology, vol. 219, no. 1, pp. 176-185, 2001.

[49] K. Hynynen, G. Clement, N. McDannold, R. King, P. White, F. Jolesz, S. Vitek, and E. Zadicario, "Pre-clinical testing of a phased array ultrasound system for mri-guided noninvasive surgery of the brain," in Proceedings of the Eleventh Meeting of the International Society for Magnetic Resonance in Medicine, Toronto, ON, p. 77, 2003.

[50] E. J. Schmidt, V. K. Reddy, and J. N. Ruskin, "Nonenhanced magnetic resonance imaging for characterization of acute and subacute radiofrequency ablation lesions," Heart Rhythm, vol. 4, no. 2, pp. 215-217, 2007.

[51] S. Gabriel, R. Lau, and C. Gabriel, "The dielectric properties of biological tissues: Iii. parametric models for the dielectric spectrum of tissues," Physics in medicine and biology, vol. 41, no. 11, p. 2271, 1996.

[52] Persson, Mikael and Fhager, Andreas and Trefna, Hana Dobsicek and Takook, Pegah and Yu, Yinan and McKelvey, Tomas and Karlsson, Jan-Erik and Zeng, Xuezhi and Zirath, Herbert and Elam, Mikael, "Microwave based diagnostics and treatment in practice," Microwave Workshop Series on RF and Wireless Technologies for Biomedical and Healthcare Applications (IMWS-BIO), 2013 IEEE MTT-S International.

[53] S. Li, "Fast imaging reconstruction in microwave tomography for stroke diagnosis," 2013.

[54] G. Sreenivasa, J. Gellermann, B. Rau, J. Nadobny, P. Schlag, P. Deuflhard, R. Felix, and P. Wust, "Clinical application of the hyperthermia treatment planning system hyperplan–comparison of algorithms and clinical observables," Int J Radiat Oncol Biol Phys, vol. 55, pp. 407-419, 2003.

[55] C. Rigato, "Design of hyperthermia applicator for head and neck tumour cancer treatment: A simulation study," 2013.

[56] M. Paulides, D. Wielheesen, J. Van Der Zee, and G. Van Rhoon, "Assessment of the local sar distortion by major anatomical structures in a cylindrical neck phantom," International journal of hyperthermia, vol. 21, no. 2, pp. 125-140, 2005.

[57] Y. Gouda, "Microwave-based temperature monitoring: Sensitivity to temperature changes," 2013.

[58] A. Fhager, Microwave tomography. Doktorsavhandlingar vid Chalmers tekniska högskola. Ny serie, no: 2468, Institutionen för signaler och system, Biomedicinsk elektromagnetik, Chalmers tekniska högskola, 2006. 135.
[59] Y. cell. [Online]. Available: http://fdtd.wikispaces.com/The+Yee+Cell.

A

Basic definitions

A.1 Maxwell's equations

The most common way to describe the theory of electromagnetics is a set of coupled partial differential equations, known as Maxwell's equations [3]:

$$\nabla \times \mathbf{E} = -\mu \frac{\partial H}{\partial t}, \tag{A.1}$$

$$\nabla \times \mathbf{H} = -\sigma E + \varepsilon \frac{\partial E}{\partial t}, \tag{A.2}$$

$$\nabla \cdot \epsilon E = \rho, \tag{A.3}$$

$$\nabla \cdot \mu H = 0. \tag{A.4}$$

where $\mathbf{E}$ is the electric field intensity, $\mathbf{H}$ the magnetic field intensity, μ the permeability, ρ the electric charge density, the permittivity and σ the conductivity. Maxwell's equations can be used to explain all the classical electromagnetic phenomena together with Lorentz's force law (Eq. A.5) and the continuity equation (Eq. A.6):

$$f = \nabla \cdot \sigma - \frac{1}{c^2} \frac{\partial S}{\partial t}, \tag{A.5}$$

$$\nabla \cdot \mathbf{J} = -\frac{\partial \rho}{\partial t}, \tag{A.6}$$

The current density is denoted $\mathbf{J}$ and the speed of light $c(\frac{1}{\sqrt{\epsilon\mu}})$, S denotes directional energy flux density (the rate of energy transfer per unit area) of an electromagnetic field.

A.2 The FDTD method

Maxwell's equations are usually used as an analytical solution only for simple geometries. For more complicated problems it is impossible to use this analytical solution, therefore a well-known numerical solver method is the finite difference time-domain (FDTD) method [58]. This method uses regular Cartesian meshes for the electric and magnetic fields and the E- and H-field components are placed in the center of a 3D space (Figure A.1). This model is known as Yee cell which shows a numerical solution of initial boundary value problems.

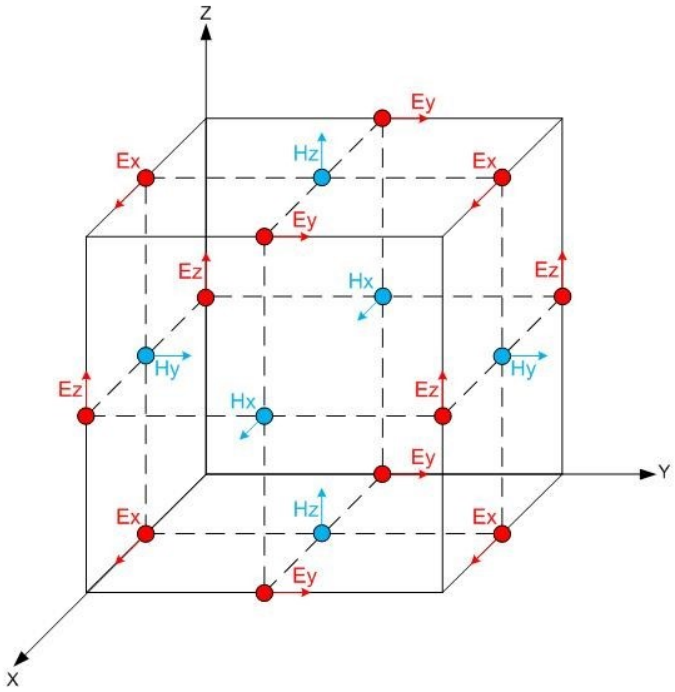

Figure A.1: The Yee cell model [59].

From the equations (A.1) and (A.2) and also by considering the Yee cell method, the following six equations can be written:

$$\frac{\partial H_x}{\partial t} = \frac{1}{\mu}(\frac{\partial E_y}{\partial z} - \frac{\partial E_z}{\partial y} - \sigma H_x), \tag{A.7}$$

$$\frac{\partial H_y}{\partial t} = \frac{1}{\mu}(\frac{\partial E_z}{\partial x} - \frac{\partial E_x}{\partial z} - \sigma H_y), \tag{A.8}$$

$$\frac{\partial H_z}{\partial t} = \frac{1}{\mu}(\frac{\partial E_x}{\partial y} - \frac{\partial E_y}{\partial x} - \sigma H_z) \tag{A.9}$$

$$\frac{\partial E_x}{\partial t} = \frac{1}{\epsilon}(\frac{\partial H_z}{\partial y} - \frac{\partial H_y}{\partial z} - \sigma E_x), \tag{A.10}$$

$$\frac{\partial E_y}{\partial t} = \frac{1}{\epsilon}(\frac{\partial H_x}{\partial z} - \frac{\partial H_z}{\partial x} - \sigma E_y), \tag{A.11}$$

$$\frac{\partial E_z}{\partial t} = \frac{1}{\epsilon}(\frac{\partial H_y}{\partial x} - \frac{\partial H_x}{\partial y} - \sigma E_z) \tag{A.12}$$

B

Equivalent dielectric properties

The Table B.1 presents the dielectric properties for muscle tissue at different temperature. Also, Figure B.2 shows the equivalent simulations for the given dielectric properties at the center of the phantom. Different colors are used to indicate the temperature differences in each simulation.

Temperature	Frequency (GHz)	Permittivity (*Eps'*)	(*Eps''*)
20 ℃	0.1	65.9724	127.1927
	0.5	56.9527	34.1456
	1.0	54.6774	16.9010
	1.5	53.6680	13.5891
	2.0	53.2476	13.0261
25 ℃	0.1	73.3017	81.5067
	0.5	66.6263	24.3473
	1.0	64.0421	18.0961
	1.5	61.4984	18.0145
	2.0	59.1742	18.2301
30 ℃	0.1	74.6363	98.6564
	0.5	65.9414	26.2467
	1.0	63.5088	18.5568
	1.5	61.3233	17.8294
	2.0	59.2611	17.7970
35 ℃	0.1	76.1007	116.3102
	0.5	65.1748	28.5691
	1.0	62.8447	19.1105
	1.5	60.9652	17.6807
	2.0	59.2000	17.4184
40 ℃	0.1	77.6188	134.9288
	0.5	64.4280	30.9861
	1.0	62.1083	19.9681
	1.5	60.4665	17.8112
	2.0	58.9991	17.1088
45 ℃	0.1	80.8147	160.5072
	0.5	63.4794	33.9024
	1.0	61.1266	21.1727
	1.5	60.2224	17.6150
	2.0	58.5320	17.0391

Figure B.1: Equivalent dielectric properties of muscle phantom for different temperatures.

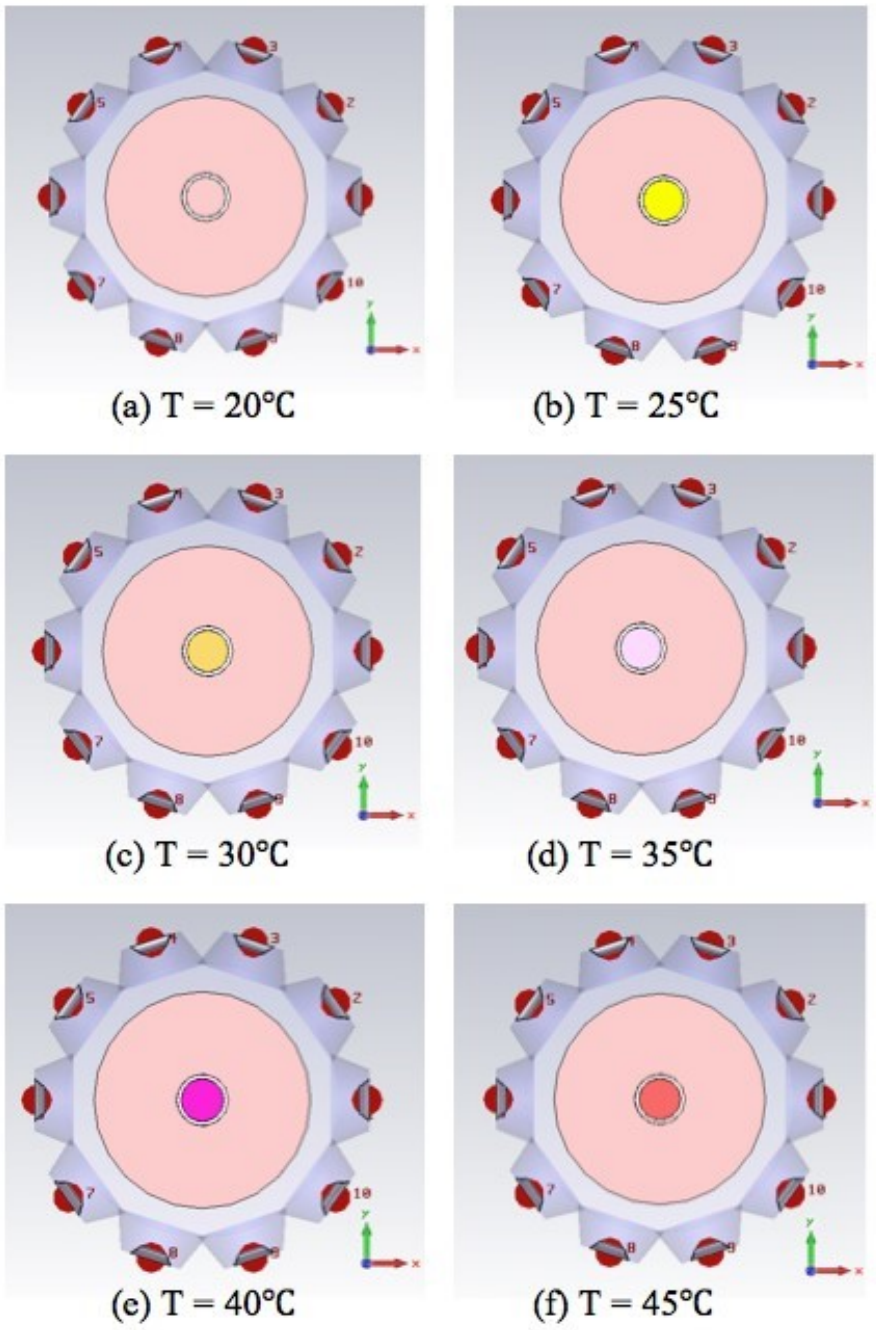

Figure B.2: The simulated muscle phantom for different temperatures.

C

More plots for amplitude-based Good Data Ratio

In this section more results are plotted for: the system amplitude error for various tube sizes (C.3), the system phase error for various temperature differences (C.1) and the system amplitude and phase error for various temperature differences (C.2).

C.1 System phase error for various temperature differences

a) MW tomography simulation

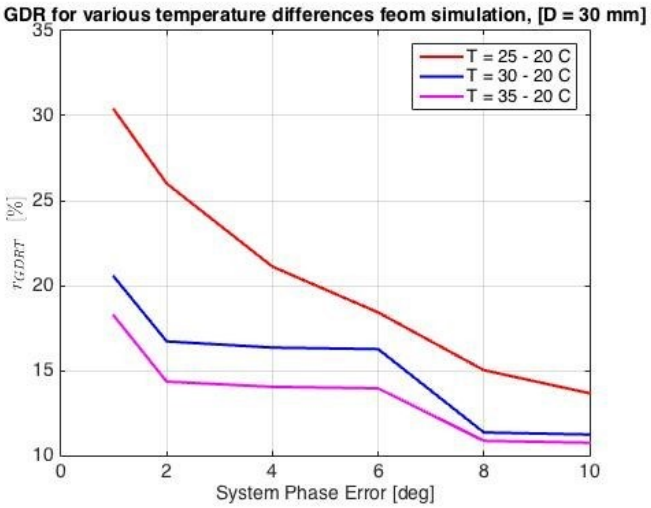

Figure C.1: The GDR% as a function of phase system error for the simulated MW tomography system.

b) MW tomography measurement

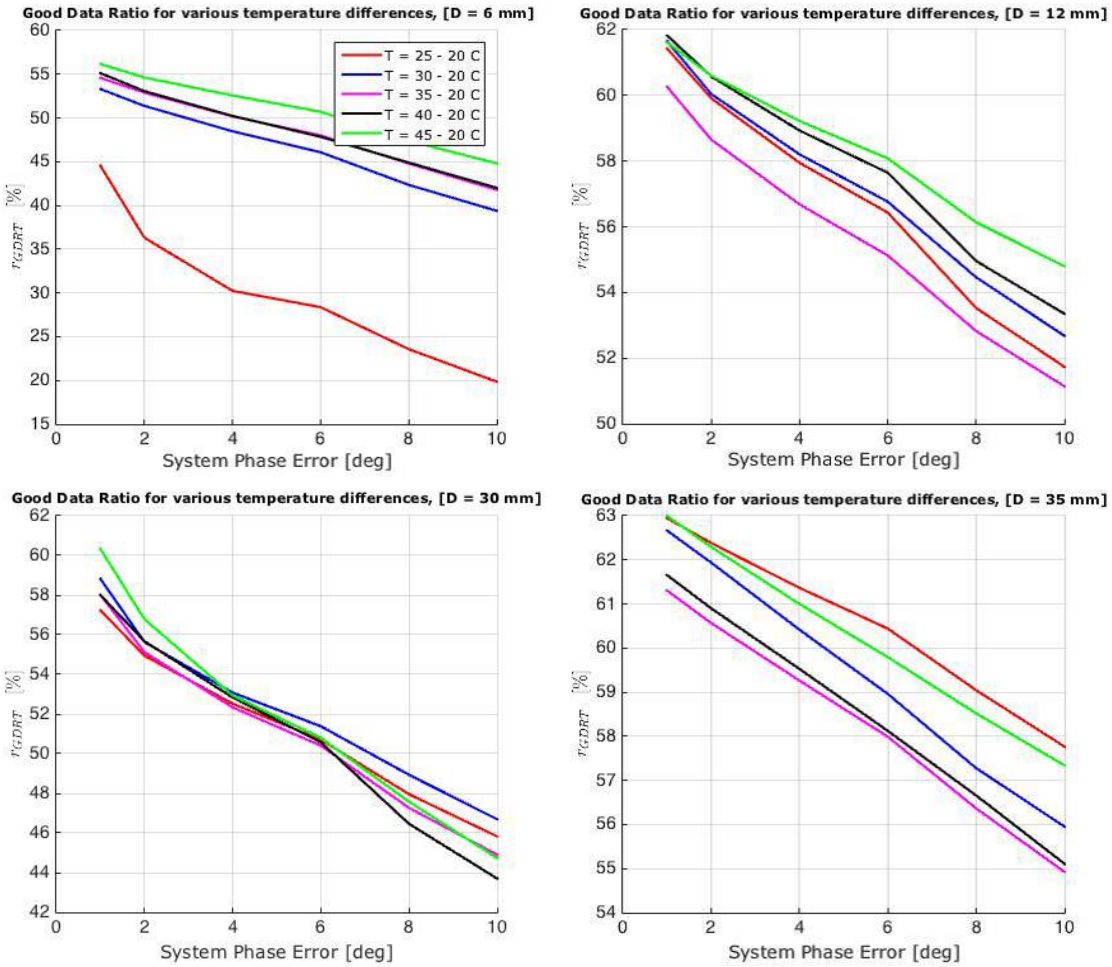

Figure C.2: The GDR% for various tube sizes as a function of the system phase error for the experimental MW tomography setup.

c) HT applicator simulation

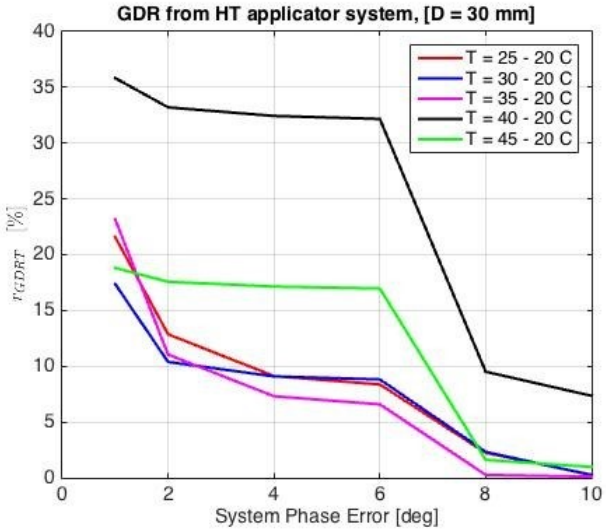

Figure C.3: The GDR% as a function of phase system error for the simulated HT applicator system.

C.2 System amplitude and phase-based GDR(%) for various temperature differences

a) MW tomography simulation

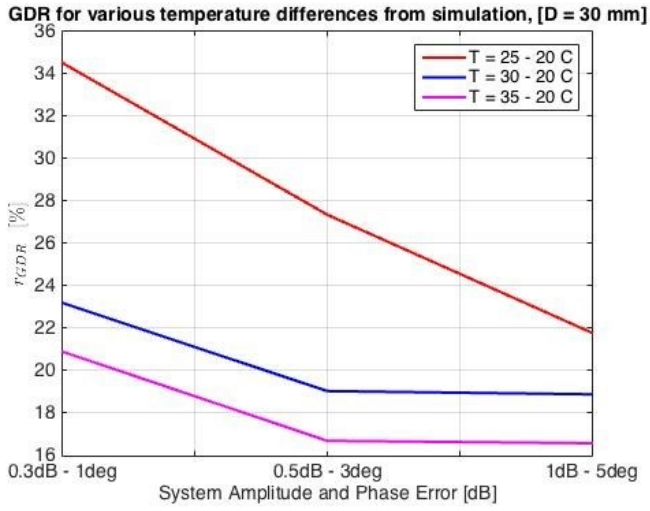

Figure C.4: The GDR% as a function of phase system error for the simulated HT applicator system.

b) MW tomography measurement

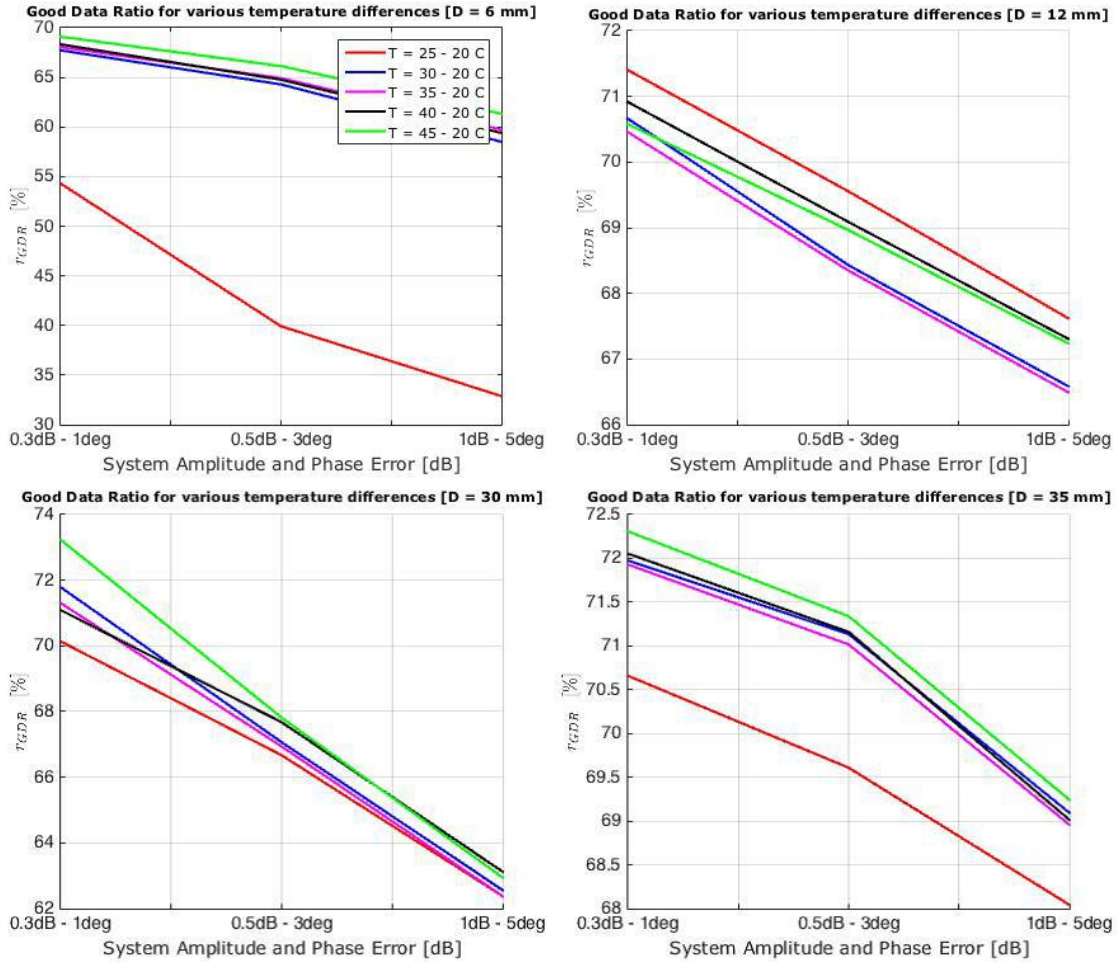

Figure C.5: The GDR% for various tube sizes, as a function of the system amplitude and phase error.

c) HT applicator simulation

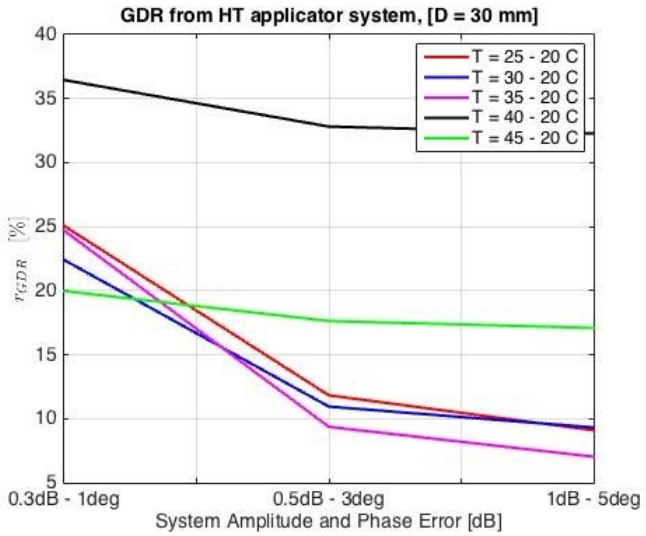

Figure C.6: The GDR% as a function of amplitude and phase system error for the simulated HT applicator system.

C.3 System amplitude error for various tube sizes for MW tomography measurement

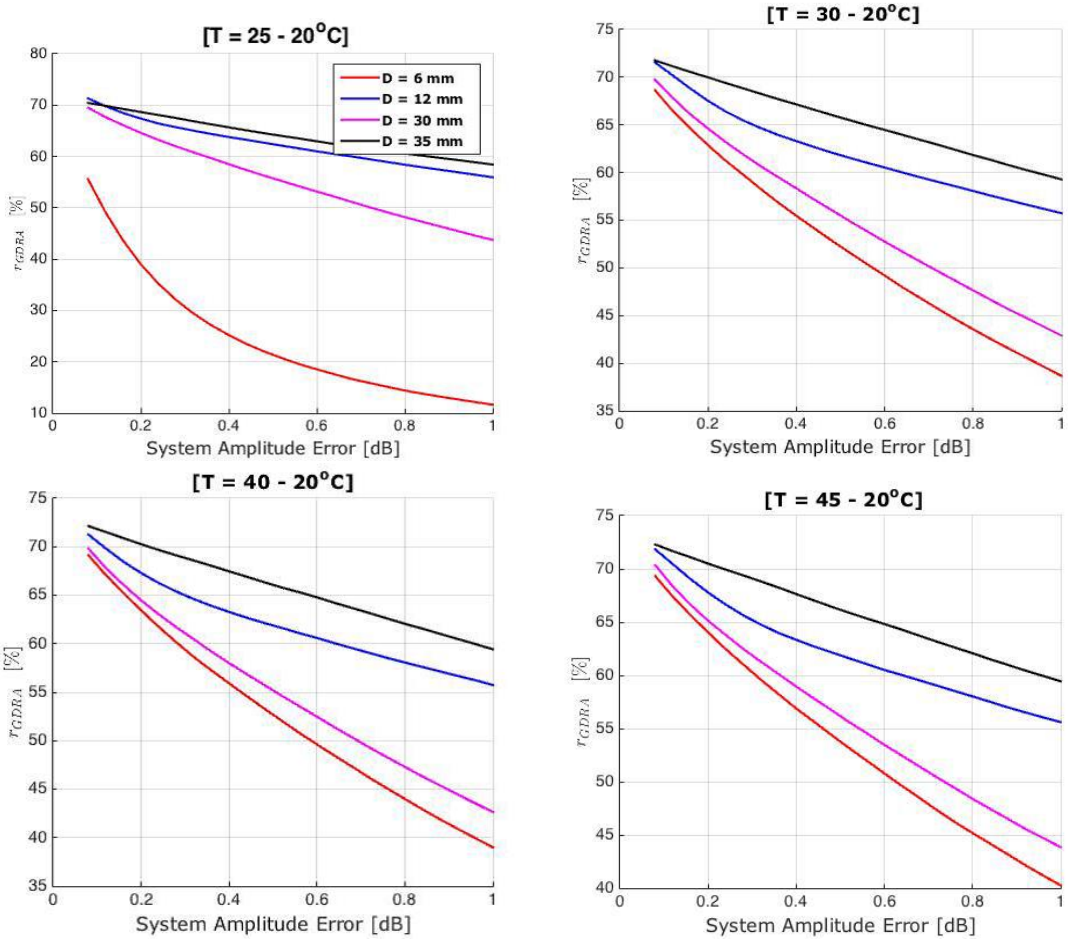

Figure C.7: The GDR% for various tube sizes as a function of the system amplitude error.

C.4 System amplitude error for smaller temperature steps (1°C)

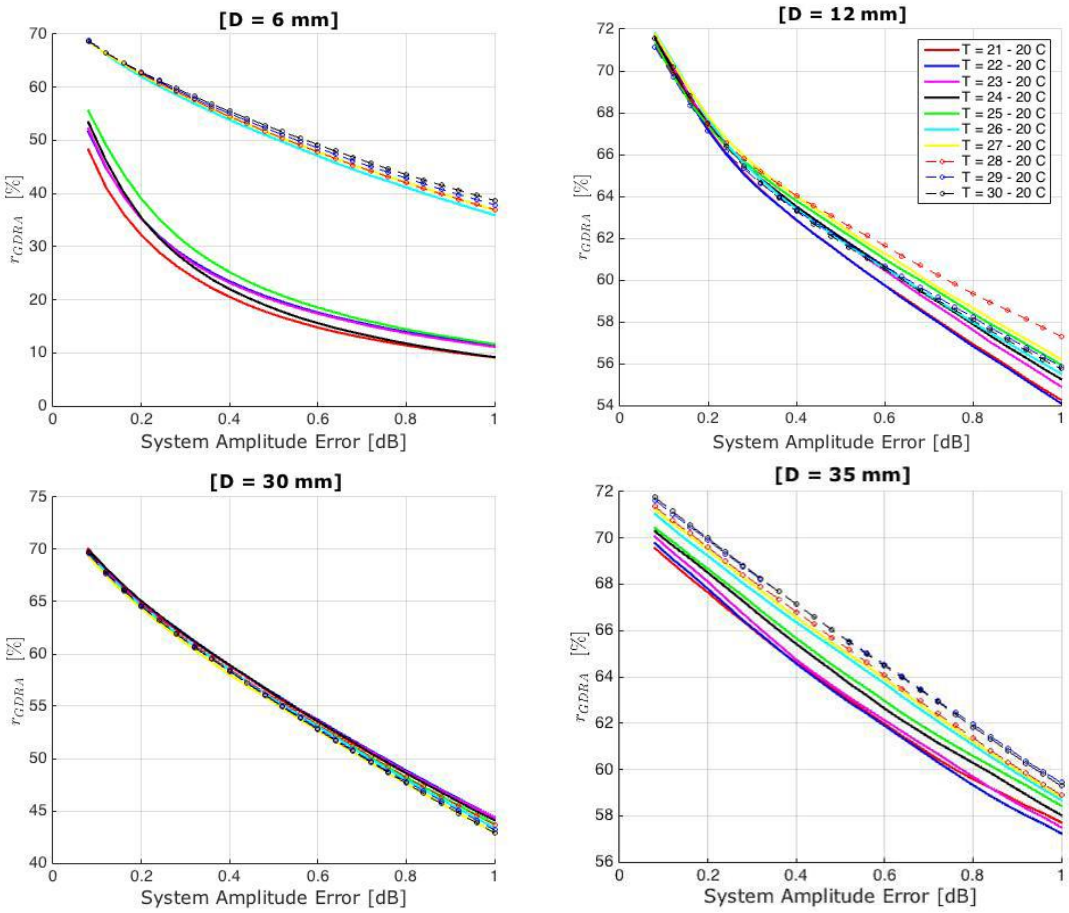

Figure C.8: The GDR% for various temperature differences with 1°C steps